

**ALUMINUM BASED NANOSENSORS FOR ULTRASENSITIVE
BIO-DETECTION**

by

Sri Sankari Ganesan

Bachelor of Engineering, Anna University, 2016

A thesis

presented to Ryerson University

in partial fulfilment of the

requirements for the degree of

Master of Applied Science

in the program of

Aerospace Engineering

Toronto, Ontario, Canada 2019

© Sri Sankari Ganesan, 2019

AUTHOR'S DECLARATION FOR ELECTRONIC SUBMISSION OF A THESIS

I hereby declare that I am the sole author of this thesis. This is a true copy of the thesis, including any required final revisions, as accepted by my examiners.

I authorize Ryerson University to lend this thesis to other institutions or individuals for the purpose of scholarly research.

I further authorize Ryerson University to reproduce this thesis by photocopying or by other means, in total or in part, at the request of other institutions or individuals for the purpose of scholarly research.

I understand that my thesis may be made electronically available to the public.

ALUMINUM BASED NANOSENSORS FOR ULTRASENSITIVE BIO-DETECTION

Sri Sankari Ganesan

Master of Applied Science, Aerospace Engineering, Ryerson University, Toronto (2019)

ABSTRACT

A 3-dimensional, biocompatible Aluminum based nanomaterial with tunable morphological properties is fabricated using Femtosecond Pulsed Laser system. The novel material synthesized is characterized to define its physical and optical properties owing to its purpose in the desired field. Two unique shapes of Aluminum nanostructures, multifaceted and spherical, are defined and are tested for Raman activity in SERS based applications. The nanoprobles are analysed in the field of chemical sensing using Crystal Violet and Rhodamine 6G and bio-sensing using cysteine and carcinoembryonic antigen. The nanoprobles possess the ability of SERS excitation up to single molecule sensing. The research is extended to in-vitro cancer diagnosis by its ability to sense the intracellular biomarkers produced by the cancer cells. Three cell lines are evaluated, mammalian fibroblast and pancreatic and lung cancer cells, for which further analysis is performed to prove the viability of the nanoprobles to differentiate between cancerous and non-cancerous cells by implementing ratio analysis on the obtained SERS spectrum.

ACKNOWLEDGEMENTS

First and foremost, I express my sincere gratitude to my research supervisors Dr. Bo Tan and Dr. Krishnan Venkatakrishnan for granting me the prospect of pursuing my research program and for consistently supporting and guiding me all through the progress.

I would also like to thank my friends and fellow lab-mates who had immensely helped me with research experiments and concepts.

Ultimately, I would like to thank my family members for their love, support and prayers and dedicate my thesis to my parents without whom this wouldn't have been possible.

TABLE OF CONTENTS

Author's declaration	ii
Acknowledgements	iv
List of Figures	vii
List of Tables.....	vii
List of Abbreviations.....	xi
CHAPTER 1	1
INTRODUCTION	1
1.1 Aluminum nanoparticles	1
1.1.1 Aluminum nanoparticle synthesis	3
1.2 Alumina nanoparticles.....	3
1.2.1 Phases of Alumina.....	3
1.2.2 Synthesis of Al ₂ O ₃ nanoparticles.....	4
1.2.3 Laser synthesis of Al/Al ₂ O ₃ nanoparticles	4
1.3 Al/Al ₂ O ₃ particle for Raman Spectroscopy and SERS	5
1.4 Aluminum/Alumina in cellular application.....	6
1.5 Research scope and Objective.....	7
CHAPTER 2	8
EXPERIMENTAL METHOD.....	8
2.1 Laser ablation and material	8
2.2 Material characterization.....	8
2.3 Raman Sensing.....	8
2.4 Cell culture, sensing and analysis	9
CHAPTER 3	11
FABRICATION AND CHARACTERIZATION OF ALUMINUM BASED NANOSTRUCTURES	11
3.2 Morphological characterization of Aluminum/Aluminum oxide.....	13
3.2.1 Size of Aluminum/Alumina nanostructures	16
3.2.2 Composition of the nanostructure.....	18
3.2.3 Lattice spacing of Aluminum/Alumina	21

3.3 Optical properties of Aluminum/Aluminum Oxide.....	24
3.3.1 Raman spectrum of Aluminum/Alumina	25
3.4 Summary	29
CHAPTER 4	30
SERS BASED MOLECULAR DETECTION.....	30
4.1 Introduction	30
4.2 Limit of Detection	42
4.3 Summary	43
CHAPTER 5	43
ALUMINUM BASED SERS PROBE FOR IN-VITRO CANCER DETECTION	44
5.1 Introduction	44
5.2 Material preparation for cell culture.....	44
5.3 Cell seeding and fixation.....	44
5.4 Cells under fluorescence microscope	45
5.5 Cell sensing using Raman Spectroscopy.....	46
5.6 Time study of SERS in cancerous and non-cancerous cells	48
5.7 Summary	50
CONCLUSION AND FUTURE RESEARCH.....	51
Conclusion.....	50
Future Research.....	52
Appendix.....	53
REFERENCES	55

LIST OF TABLES

Table 3.1 Composition of element present in of a) multifaceted nanostructures b) spherical nanostructures	20
Table 3.2 d-spacing for Aluminum/Aluminum oxide and the corresponding planes.....	22
Table 4.1 Observed peaks of Crystal Violet with peak assignments from literature.....	34
Table 4.2 Observed peaks of Rhodamine 6 G with peak assignments from literature cm^{-1}	37
Table 4.3 Observed peaks of Cysteine with peak assignments from literature cm^{-1}	39

LIST OF FIGURES

Figure 1.1 Aluminum nanoparticles at 300000x magnification highlighting the amorphous oxide shell surrounding the crystalline core	2
Figure 3.1 Femtosecond laser ablation of Al substrate and fibrous nanostructures (SEM and HRTEM) formation	11
Figure 3.2 Self assembled 3D Aluminum/Alumina nanoparticles formed at different laser conditions.....	13
Figure 3.3 a) and b) SEM imaging c) FESEM image (d) – (f) HRTEM images.....	14
Figure 3.4 HRTEM image showing the d spacing orientation in different planes in the same structure (2MHz).....	15
Figure 3.5 a) Cubic crystal structure of Alumina (gamma) b) Hexagonal Crystal Plane structure of Alumina (alpha).....	16
Figure 3.6 TEM images and the corresponding size distribution of nanoparticles for (a-c) multifaceted structures (high peak power) (d-f) spherical structures (low peak power), (g-i) Combination of multifaceted and spherical structures (with Nitrogen gas)	18
Figure 3.7 EDX for the fabricated sample spherical nanostructures (left) and multifaceted nanostructures (right).....	19
Figure 3.8 XPS data of a) multifaceted nanostructures b) spherical nanostructures	19
Figure 3.9 Lattice spacing values calculated for various crystal orientation (HRTEM images) for multifaceted nanostructures	21
Figure 3.10 Lattice spacing values calculated for various crystal orientation (HRTEM images) for spherical nanostructures	22
Figure 3.11 SAED pattern showing a crystalline-amorphous structure	23
Figure 3.12 SAED showing a) crystalline b) amorphous and c) crystalline-amorphous phase coexistence on the same sample at different points	23
Figure 3.13 UV-Vis spectrum of Aluminum/Alumina a) in ethanol b) in ethanol with CV	24
Figure 3.14 Tauc plot to determine the band gap	25
Figure 3.15 Raman spectra of a) bare Aluminum substrate and b) nanofabricated substrate (multifaceted nanostructures) c) nanofabricated substrate (spherical nanostructures)	26

Figure 3.16 Raman spectrum for sample fabricated at a higher ionization energy (multifaceted nanostructures).....	26
Figure 3.17 Raman spectrum for sample fabricated at a lower ionization energy (spherical nanostructures).....	27
Figure 3.18 Crystal structure of Alumina a) gamma phase b) alpha phase with Oxygen vacancies based on experimental data.....	28
Figure 3.19 Multi-crystalline-amorphous grain structure of Alumina.....	28
Figure 4.1 Electromagnetic enhancement mechanism of Aluminum nanostructures by Tip enhanced Raman Spectroscopy.....	30
Figure 4.2 Charge transfer mechanism induced by the incident photon, electrons transferred to molecular orbitals of analyte molecules	31
Figure 4.3 Raman spectra of CV adsorbed on Al nanostructure at 532nm wavelength on multifaceted nanostructure.....	32
Figure 4.4 Raman spectra of CV adsorbed on Al nanostructure at 785nm wavelength on a) multifaceted nanostructure, b) spherical nanostructure c)spherical-multifaceted nanostructure..	33
Figure 4.5 Enhancement factor with varying concentration for CV adsorbed on multifaceted nanostructures	35
Figure 4.6 Raman spectra of R6G adsorbed on Al nanostructure at 532nm wavelength on multifaceted nanostructure.....	35
Figure 4.7 Raman spectra of R6G adsorbed on Al nanostructure at 785 nm wavelength on a) multifaceted nanostructure b) spherical nanostructures c) spherical-multifaceted nanostructure	36
Figure 4.8 Enhancement factor with varying concentration for R6G adsorbed on multifaceted nanostructures	38
Figure 4.9 EF values comparison for different morphology of nanostructures.....	38
Figure 4.10 Raman spectra of cysteine adsorbed @ 532nm wavelength on a) multifaceted b) spherical Al nanostructure c)cysteine molecular structure d) SERS mechanism of cysteine adsorbed on spherical and multifaceted nanostructure	40
Figure 4.11 Raman spectra of CEA adsorbed on Al nanostructures of various modes @ a) 532 nm b) 785 nm c) molecular structure of CEA d) SERS mechanism of CEA adsorbed on multifaceted and spherical structures.....	41

Figure 5.1 Fluorescence imaging of cells on spherical and multifaceted nanostructures.....	46
Figure 5.2 Raman vs SERS signals for cancerous and non-cancerous cells and their corresponding fluorescence images	47
Figure 5.3 Raman spectrum of cells seeded on different shapes of nanostructures compared with the cells seeded on plain Aluminum substrate at 532nm	48
Figure 5.4 Time study carried out at 6h, 18h, 24h,amd 48h for cancerous and non-cancerous cell lines seeded on multifaceted and spherical nanostructures.....	49
Figure 5.5 Ratio analysis for classification of cells	50

LIST OF ABBREVIATIONS

ATCC – American Type Culture Collection
CEA – Carcino Embryonic Antigen
CL – Cathodoluminescence
CV – Crystal Violet
DMEM – Dulbecco’s Modified Eagle Medium
DNA – Deoxyribonucleic acid
EDX – Electron Dispersive X-ray
EELS – Electron Energy Loss Spectroscopy
EM – Electromagnetic
FESEM – Field Emission Scanning Electron Microscopy
FBS – Fetal Bovine Serum
FFT – Fast Fourier Transform
fs - Femtosecond
HRSEM – High Resolution Scanning Electron Microscopy
HRTEM – High Resolution Transmission Electron Microscopy
IR – Infra-Red
LSPR – Localized Surface Plasmon Resonance
nm – Nanometer
R6G – Rhodamine 6 G
SEIRA – Surface Enhanced Infrared Absorption Spectroscopy
SEM – Scanning Electron Microscopy
SERS – Surface Enhanced Raman Spectroscopy
UV – Ultra Violet
XPS - X-ray Photoelectron Spectrometry

CHAPTER 1 INTRODUCTION

The most abundant metal in the earth's crust, Aluminum, has significantly attracted interest in nanoscale synthesis due to the plasmon activity extended from the UV to the near-IR region[1][2][3] of the spectrum. as its size is increased respectively. Aluminum nanostructures are known for their greatly reduced cost, easy fabrication, high surface area and reactivity and inherent sustainability and are being used for several potential applications in the biomedical field[2]. Other promising applications of these nanostructures include photo-catalysis[3][4], photo-detection[3]–[6], combustible additives in propellant[7] and sensing including surface-enhanced spectroscopies[2][4], which include localized surface plasmon resonance (LSPR) sensing, surface-enhanced infrared absorption spectroscopy (SEIRA) and surface-enhanced Raman spectroscopy (SERS). The following is a short review of previous works on Aluminum based nanomaterials and their applications pertaining to the field of SERS and cell-based studies.

1.1 ALUMINUM NANOPARTICLES

Nanoparticles fabricated using Aluminum metal isn't unheard of and these particles are known for their consistency and reproducibility. Their unique properties finds application in many fields which includes utilising them as fuel/propellant due to their high surface reactivity, high energy density and heat of reaction to form Al_2O_3 [7]. They are also good plasmonic metals which present sharp localized surface plasmon resonances (LSPRs) extending up to the UV region[3][8][9]. The plasmon resonance of Al extends from UV up to IR with increase in size of the nanostructures. In the nanoscale Al also extends to develop a high capacity hydrogen storage material and holding a low solar radiation absorption coefficient it also acts as a good insulator to store the energy[7][10]. The sensing capability of Aluminum is said to be limited owing to its intrinsic property of possessing a large imaginary part of dielectric constant[8].

For several decades, the optical properties of nanometallic particles have been studied, though at first in the visible and infrared spectra, more recently the studies have been extended in the UV region. These optical properties are well dominated by the collective electron oscillations at the metal dielectric interface known as surface plasmons. In a metallic nanoparticle these electron oscillations are confined inside the boundaries of the particle, which can be tuned by shaping the geometry, resizing the nanoparticle or changing the dielectric environment[11].

The optical properties of individual Al nanocrystals can be measured using dark-field spectroscopy, cathodoluminescence (CL), and electron-energy loss spectroscopy (EELS), which clearly shows the size dependent, continuous tuning of the optical resonance from ultraviolet to the visible region of the spectrum with increasing nanocrystal diameter[1][12]. A distinguishing feature of Al nanocrystals is their thin, stable, amorphous surface oxide layer that inhibits further oxidation of the metal. The Al nanocrystals are terminated by this self-limiting oxide layer, which imparts stability, an important property that can ultimately enable their use in many different types of applications.

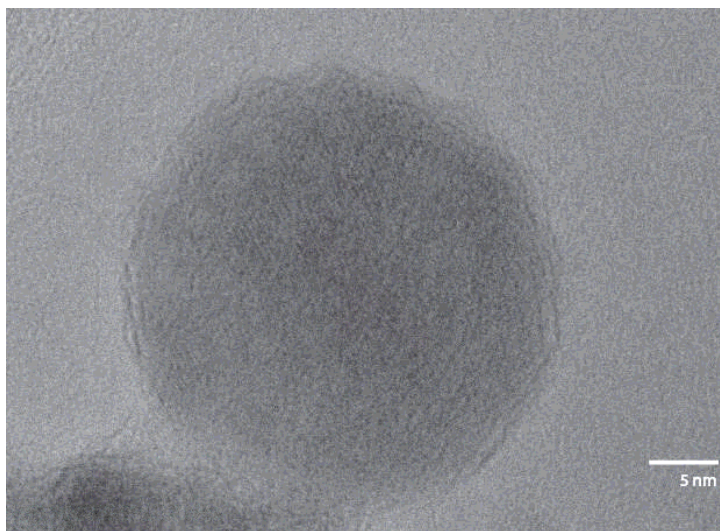


Figure 1.1 Aluminum nanoparticles at 300000x magnification highlighting the amorphous oxide shell surrounding the crystalline core

Aluminum nanocrystal aggregates are reported to be capable of substantial near-infrared SERS enhancements, similar to gold and silver nanoparticles. The interaction between the substrate and molecules for an Al nanoparticle oxidized at the surface level differs dramatically from that of noble metal substrates [4]. Another interesting note is that the plasma frequency of Aluminum is higher than that of noble metals enabling the metal to exhibit plasmon resonances extended up to the UV range as well [9]. Al nanoparticle arrays fabricated over wide areas in a well-defined manner using extreme-UV interference lithography exhibits sharp and tunable plasmon resonances in the UV and deep-UV wavelength ranges[13]. Thus far, SERS substrates based on plasmonic Al have primarily focused on nanostructures fabricated using e-beam lithography, such as nanoparticle or nanohole arrays and bowtie structures along with roughened films and gratings and

chemical synthesis of Al nanocrystals [14]. The extension of detection wavelength ranges from UV to IR makes Aluminum find application in several fields including sensing of biological compounds which exhibit strong UV absorptions.

1.1.1 ALUMINUM NANOPARTICLE SYNTHESIS

The commonly used methods to fabricate are wet-chemical synthesis[7], lithography techniques[3][9], mechanical attrition[7], vapour condensation[15], self assembled thin films[16], [17] and pulsed laser ablation in the nanosecond range under various media[18]. The lithographic techniques have several types namely, electron beam lithography, colloidal lithography, interference lithography and nanoimprint lithography. The above-mentioned fabrication techniques have their own disadvantages such as the presence of liquid media, non-tunable fabrication which cannot differentiate the phases, larger size distribution and expensive methods.

1.2 ALUMINA NANOPARTICLES

Aluminum always rapidly oxidizes when exposed to atmosphere with the oxygen present in the atmosphere and forms Aluminum oxide. This forms as a stable protective layer for the metal to prevent further degradation. Based on the oxidation conditions, Alumina forms various phases each of which has its distinct characteristic properties.

1.2.1 PHASES OF ALUMINA

Alumina (Al_2O_3) exist in various crystalline forms such as gamma, delta, theta and alpha phases. It has a wide bandgap which increases with increasing crystallinity and falls within the range of 3.2 eV to 8.7 eV[12][18].

γ -phase Al_2O_3 has been described to have a defect spinel with the idealized formula $\text{Al}_{2(1+1/3\varpi+2/3)}\text{O}_{32}$, where ϖ denotes a vacancy[20]. Though γ -alumina is widely being used in various complex applications, its detailed structure such as its exact vacancy distribution, surface definition and such relative are still unclear. γ -phase nano- Al_2O_3 is small in size, possess a low melting temperature and has high surface activity. This phase is said to have a rhombohedral structure and exhibits the highest bandgap of 8.7 eV. It is also said to be one of the purest forms

of alumina compared to other phases. The high surface activity of this alumina phase makes it eligible to find an application as a catalytic material by undergoing thermal melting techniques.

α-phase alumina is said to have higher with phase stability, high dimensional stability, comparatively higher hardness and this phase is being widely used in a number of ceramics, plastics, rubber products for toughening finish, fracture toughness, thermal fatigue resistance, wear and creep resistance. Alpha alumina has hexagonal crystal structure and is considered to be the most stable phase compared to other phases of Alumina. Alpha alumina is said to have higher performance in the infra-red emission as it is used for the fabrication of sapphire, ruby, Yt-Al garnet and as thermal insulating materials. As it possesses a high level of resistivity and provides good insulation, it is being used as the major component for the production of YGA crystal laser and IC substrates.

1.2.2 SYNTHESIS OF AL₂O₃ NANOPARTICLES

Al have primarily focused on nanostructures fabricated using e-beam lithography, such as nanoparticle or nanohole arrays and bowtie structures, along with roughened films and gratings. Chemical methods for the synthesis of Al nanoparticles have involved the thermal decomposition of an aluminum hydride with a titanium catalyst but size and shape control have proven to be problematic with this approach. The facile synthesis of highly regular, faceted aluminum nanocrystals with controllable nanocrystal diameters ranging from 70 to greater than 200 nm.

1.2.3 LASER SYNTHESIS OF AL/AL₂O₃ NANOPARTICLES

Pulsed laser ablation is said to be one of the first technique developed to mass produce Al nanoparticles. Major studies reported Al/Alumina nanoparticles fabrication using nanosecond pulsed laser ablation technique under different media conditions. There have also been a few experiments reported with ps and fs laser ablation with Ti:Saph laser and Nd:YAG laser. The main disadvantage of fabricating nanostructures under liquid media is its photoluminescence effect and the plasmon resonance is mainly located only in the UV part of the spectrum. Al microhole arrays were created by firing a train of femtosecond laser pulses at megahertz pulse frequency onto the surface of an aluminum target. The laser trains ablated the target surface and created microholes leading to the generation of deposited nanostructures inside and around the microholes. Several laser synthesis methods involved ablation of the substrates in solution and not in ambient

condition. Also, the pulsed laser synthesis of Al/Alumina has not been developed for plasmonic applications

1.3 AL/AL₂O₃ PARTICLE FOR RAMAN SPECTROSCOPY AND SERS

Raman spectroscopy proves to be an important analytical technique which provides information on molecular bonds on the basis of their distinctive vibrational signatures. However, its application at low analyte concentrations is limited by the inherently low Raman cross sections. Surface-enhanced Raman scattering (SERS) has emerged as an important technique for enhancing the Raman scattering cross section. Since the advent of SERS in the 1970s, it has been primarily been associated with mainly noble metal substrates composed of nanostructures. The weak Raman scattering signals are substantially enhanced in the existence of a nanostructured metallic surface next to a specimen. Surface-enhanced Raman scattering (SERS) results when nanostructured metallic substrates locally amplify electromagnetic fields at or near the substrate surfaces upon photon excitation. Enhancement of the electromagnetic (EM) field at the metal nanoparticle surface due to the excitation of localized surface plasmon resonance (LSPR) in a metal nanostructure is considered to be the dominant SERS enhancement mechanism. Molecules on the metal surface or in close proximity to it experiences the increased EM near-field and therefore scatter more efficiently. With recent advancements in the fabrication of metal nanostructures and improved detection techniques, SERS has emerged as a technique capable of ultrasensitive detection down to a single molecule.

The thin oxide surface layer in Al nanoparticles are seen as quite advantageous for SERS as these nanoscale surface oxide layers can provide binding sites for a variety of functional groups such as carboxylic/phosphoric acids, silanes, and amides, providing very different molecule–substrate interactions relative to conventional Au or Ag SERS substrates. For Al, its intrinsic nanoscale surface oxide layer expands the types of molecules that can be bound to its surface relative to noble metals, where molecules are commonly functionalized with thiol or amine groups to facilitate molecule–substrate binding. The oxide layer can enable the SERS detection of a wider range of non-resonant molecules, including biomolecules such as DNA, where label free detection is highly desirable. Al nanocrystal substrates enable to perform the first label-free SERS compositional quantification of ssDNA without any modification to either the molecule or the substrate. In

another work, Raman measurements were performed on adenine molecules coated uniformly on the Al nanoparticle arrays at a laser excitation wavelength of 257.2 nm[4][21].

1.4 ALUMINUM/ALUMINA IN CELLULAR APPLICATION

Endothelial cells were exposed to alumina nanoparticles, measured to be around 10–20nm, at various concentrations and times. Two types of endothelial cells namely porcine pulmonary artery endothelial cells and human umbilical vein endothelial cells showed increased mRNA and protein expression of VCAM-1, ICAM-1, and ELAM-1. Furthermore, human endothelial cells treated with alumina particles showed increased adhesion of activated monocytes. The alumina particles tended to agglomerate at physiological pH in serum-containing media, which led to a range of particle sizes from nano to micron size during treatment conditions. These data show that alumina nanoparticles can elicit a pro-inflammatory response and thus present a cardiovascular disease risk [22].

In a research, an etched aluminum foil sputtered with 20nm thick gold is used for in vitro application as a base substrate and in vivo applications use it as a sacrificial substrate. When Surface Enhanced Raman Scattering is performed on these samples an enhancement of up to 10^6 is achieved[23].

In another work, reversible binding with specific alignment was observed with pepsin as a model enzyme on alumina NPs through the interaction of the phosphoryl group and the alumina surface. One phosphoryl group is attached to the Ser68 residue in the native porcine pepsin. The crystal structure of the enzyme indicates that this modified residue is positioned at the protein surface, far away from the active site that comprises Asp32 and Asp215. This feature enabled the oriented coupling of the phosphoryl group on Ser68 to alumina. Furthermore, phosphate ions in aqueous solution were found to compete with the phosphorylated protein– alumina bonds to induce the release of the enzyme. Thus, protein–alumina nanoparticle hybrids that exhibit a similar controlled-release behavior open an interesting possibility in the design of new drug-delivery methods. That is, the immobilization of functionalized therapeutic proteins on alumina nanoparticles may generate vehicles for delivery in vivo and allow the targeted release of the drug by added phosphate ions[24].

A study to observe and characterize the *in vitro* cellular effects of rat lung macrophages to exposure to aluminum oxide nanoparticles ($\text{Al}_2\text{O}_3\text{-NP}$) (30 and 40nm) compared to aluminum nanoparticles (Al-NP) (50, 80, and 120nm) was performed. This study concentrates on cell viability, mitochondrial function, phagocytosis ability, and cytokine response. Results indicate no to minimal toxicological effects on macrophages exposed as high as 500 $\mu\text{g/ml}$ for 24 hours with $\text{Al}_2\text{O}_3\text{-NP}$. However, there was a significant delayed toxicity that occurred at 96 and 144 h post exposure. Al-NP indicate slight to moderate toxicity after 24 h exposure at 100 and 250 $\mu\text{g/ml}$. The phagocytic ability of these cells was significantly hindered by exposure to each size of the Al-NP at 25 $\mu\text{g/ml}$ for 24 hours, but not by the $\text{Al}_2\text{O}_3\text{-NP}$. A series of cytokine and nitric oxide assays performed show none of these aluminum nanoparticles are inducing an inflammatory response[25].

1.5 RESEARCH SCOPE AND OBJECTIVE

Ultrashort pulsed femtosecond laser ionization of Aluminum substrates produces Al/Alumina nanoparticles, the properties of which can be tuned by controlling the laser properties. These nanostructures proffer promising applications in Raman sensing of biomolecules as well as biomedical applications such as cancer detection.

The major objective of this research is to fabricate 3D Aluminum/Alumina nanonetwork self assembled on the Aluminum substrate which can be used to sense various biomarkers present in the cancer using Raman sensing mechanism, thereby detecting cancer in human cells.

CHAPTER 2 EXPERIMENTAL METHOD

2.1 LASER ABLATION AND MATERIAL

A pulsed Ytterbium-doped fibre amplified femtosecond laser was used to fabricate the Aluminum/Alumina nanostructures. In order to maximize the control over the nanonetwork fabrication, some of the parameters of the laser need to be fixed, in this experiment the laser wavelength (1064nm), polarization (circular) were fixed while the repetition rate, the laser power and pulse width were the varying parameters. The nanostructures were created on a 10x10 array of points plotted using EzCAD software and controlled using a piezo-driven raster scanner. The Aluminum used was a 99% pure Al sheet of dimension 2.5x2.5x0.5cm and was manually smoothed from large roughness using sandpapers and treated with ethanol and air dried.

2.2 MATERIAL CHARACTERIZATION

The Aluminum nanofibers were characterized morphologically and structurally using Scanning Electron Microscope (SEM), High Resolution Scanning Electron Microscope (HRSEM) and High-Resolution Transmission Electron Microscope (HRTEM). SEM was used to confirm the presence of fibrous nanonetworks which was then further analysed using a HRSEM and HRTEM to determine the size distribution of the nanoparticles and the nanogap and the shape of the individual nanoparticle. HRTEM involves using a carbon grid to swab the sample to attach nanospheroid clusters to the grid and then the grid is scanned. It gives a magnification of up to 300000x which can provide the lattice spacing images and the shape of nanostructures. Based on the laser power and ionization potential, various areas were ablated and each were tested for corresponding shape and size.

FIJI ImageJ software was used to calculate the average size of the nanoparticles manually, which was then graphed using Origin software. Using the Fast Fourier Transform (FFT) analysis the crystal orientations present within each nanospheroids was determined using the lattice spacing values also known as d spacing.

2.3 RAMAN SENSING

Each ablation area was examined before and after a dye was coated onto the ablation using a Bruker SENTERRA Dispersive Raman Microscope at 2 different wavelengths namely 532nm and

785 nm to show multiwavelength excitation. Raman laser was used to analyze the fabricated nanostructure ablation areas to determine how the nanostructures change the Raman spectra compared to the bare unablated Aluminum substrate in terms of the Raman intensity as well as any morphological/compositional changes caused by the laser ablation. The chemical dyes used to test the SERS enhancement factor of the Aluminum nanostructures were Rhodamine 6G and Crystal Violet, which are popular dyes for SERS analysis due to their increased Raman cross-section. To determine a sensitivity range for the Al nanoweb structures, each dye was coated onto individual ablation areas at 3 different concentrations, $1 \times 10^{-3} \text{M}$ and $1 \times 10^{-6} \text{M}$. A single drop of each dye concentration for both dyes was applied to different areas ablated at various conditions prior to Raman analysis. Each resultant Raman spectra were obtained at maximum integrated time and duplicated then averaged.

In order to analyse the ability of the nanostructure to sense cancer biomarkers, Carcino Embryonic Antigen (CEA), a biomarker present in lung and colon cancer, was tested in a similar manner as that of the dyes. It was analysed at a concentration of 1 micromole ($1 \times 10^{-6} \text{M}$) at Raman wavelength of 785nm and 532nm using Bruker SENTERRA Dispersive Raman Microscope.

2.4 CELL CULTURE, SENSING AND ANALYSIS

The material having tested for Raman sensitivity is now studied to understand cell-integration on the laser transformed surface. The cell culture experiments were carried out with 2 different cell lines, pancreatic cancer cells (ASPC) and a primary mouse cell line fibroblast (NIH3T3) obtained from ATCC (American Type Culture Cultivation). The culture was performed both on the nanoparticle fabricated surface and the plain surface of Aluminum/Alumina in order to present a comparison. The cancer cell was seeded and cultured in RPMI medium supplemented with 10% Fetal Bovine Serum (FBS). These cells were incubated at 37 degree Celsius in the presence of 5% CO_2 until they reached a confluency of about 80-85%. Then, they undergo a process of trypsin wash, incubated with trypsin for 10 minutes, centrifuged and then resuspended in the RPMI medium. The fabricated Aluminum nanostructures, both multifaceted and spherical, are UV treated for 10 minutes and then placed in a petri-dish filled with 3ml RPMI media. The prepared cell in RPMI were then seeded on the nanostructures. The petri-dish was then incubated for 18,24 hours at 37 degree Celsius with 5% CO_2 . At the corresponding time, the samples were taken out, media removed and were washed with Phosphate-Buffered Saline (PBS), added with 4%

paraformaldehyde solution and incubated at room temperature for 20 minutes. The Aluminum substrate was then removed from the solution and was air dried. The process of air drying provides better sensitivity and enhancement of the SERS spectra henceforth obtained in comparison to wet samples [19].

The air-dried cell seeded samples of Aluminum substrate with nanostructures are then analysed for Raman spectrum using Renishaw inVia Confocal Raman Spectrometer. All the obtained spectrum was plotted using 'Spectragryph' spectroscopy software where it is baseline corrected and the peaks are analysed.

The cultured cells are imaged using the epi-fluorescent Nikon E-400 fluorescence microscope to detect their growth on the surface of nanostructures and image them.

CHAPTER 3 FABRICATION AND CHARACTERIZATION OF ALUMINUM BASED NANOSTRUCTURES

Physical and chemical properties of the laser synthesis aluminum-based nanostructures are characterized. It is found that the nanostructure is mixture of aluminum and alumina nanoparticles with rich defects, which give rise to unique optical and electrical properties.

3.1 ULTRASHORT LASER SYNTHESIS OF NANOSTRUCTURED ALUMINUM OXIDE

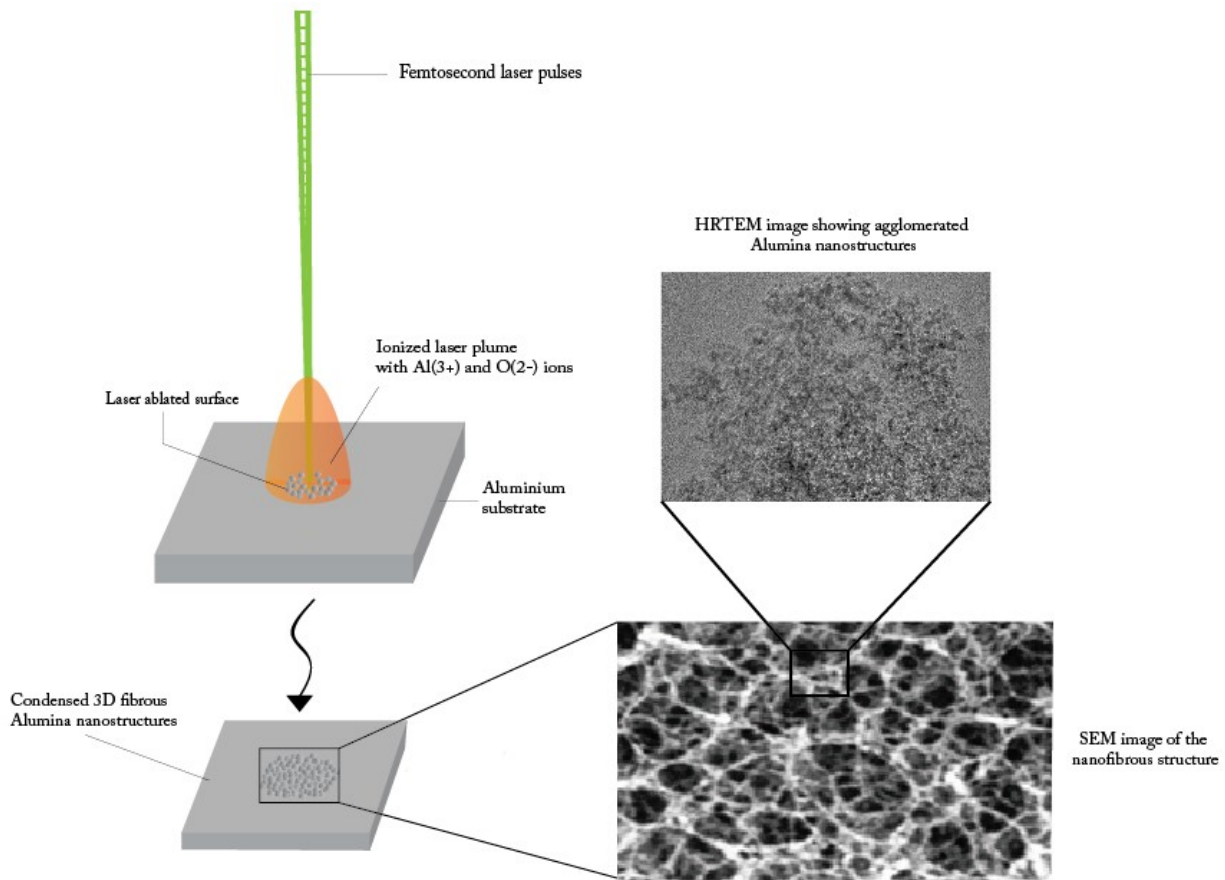


Figure 3.1 Femtosecond laser ablation of Al substrate and fibrous nanostructures (SEM and HRTEM) formation

An ionization process which transforms bulk Aluminum metal into nanostructured Aluminum Oxide is achieved using Ultrafast Femtosecond Pulsed Laser ablation of the bulk Aluminum substrates. In order to convert the bulk Aluminum substrate into nanosized Alumina crystals, the substrate is first transformed to a high energy state by exciting it with multiple photon from the

femtosecond pulsed laser. Once the atoms are in their ionized state they condense by itself and by reacting with the atmospheric oxygen. As Aluminum is highly reactive, it instantaneously combines with atmospheric gases to form interconnected web like nanostructures of Aluminum and Aluminum oxide respectively. The condensation process being time dependant, can be altered to produce a multi-crystalline and amorphous structure of nanosized Alumina with numerous grain boundaries each contributing to a different phase of Alumina. The pulsed laser is capable of creating quick shift of a range of temperature which aids in the above mentioned formation of different phases, higher temperature region aids in formation of more unorganized formation of amorphous structure while slightly less temperature provides less energy which ceases much movement and leads to a more organized manner of crystallization.

This mechanism of fabricating nanostructures is highly controllable with respect to the laser parameters, which can be manipulated to obtain nanostructures of desired geometry, phase and composition of Aluminum and its oxides. The figure 3.2 nanostructures fabricated at a higher ionization energy which has a high peak power and a lower ionization energy with low peak power. The high ionization energy condition has a low condensation time, which leads to quicker formation of Aluminum nanoparticles which thereby forms unevenly structured nanostructures leading to the formation of sharp cornered particles. On the other hand, the low ionization energy has a higher condensation time and so they can form perfectly spherical and smooth nanostructures. Also, when the pulse frequency is higher and the condensation time is low, agglomeration tends to occur more as and when compared to the low pulse frequency condition.

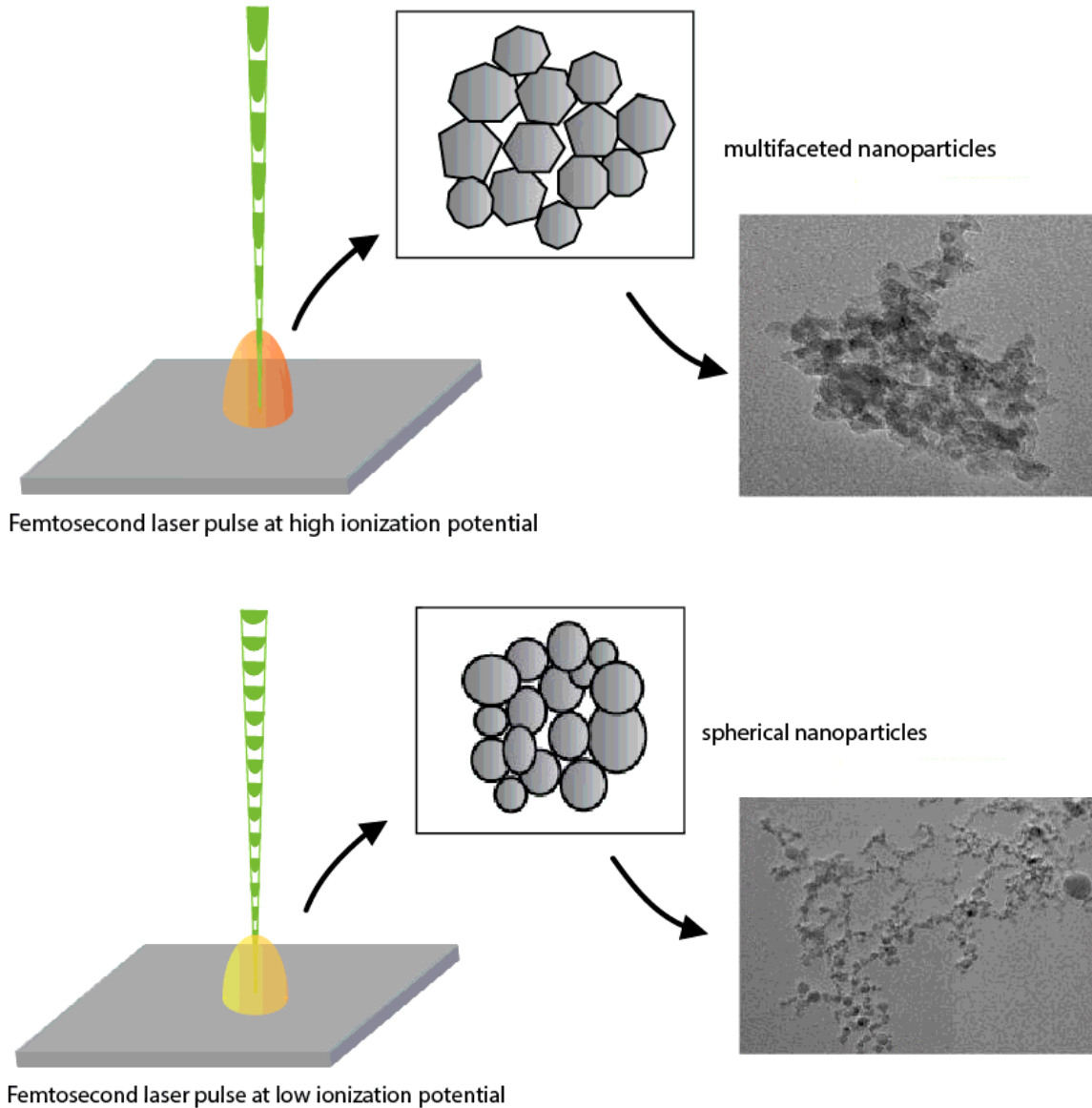


Figure 3.2 Self assembled 3D Aluminum/Alumina nanoparticles formed at different laser conditions

3.2 MORPHOLOGICAL CHARACTERIZATION OF ALUMINUM/ALUMINUM OXIDE

The multi-crystalline Aluminum/Aluminum oxide nanostructure was investigated by using microscopic and spectroscopic techniques which include Scanning Electron Microscope (SEM), High Resolution Transmission Electron Microscope (HRTEM) and Raman spectroscopy which provides information on the physical properties of Aluminum/Aluminum oxide.

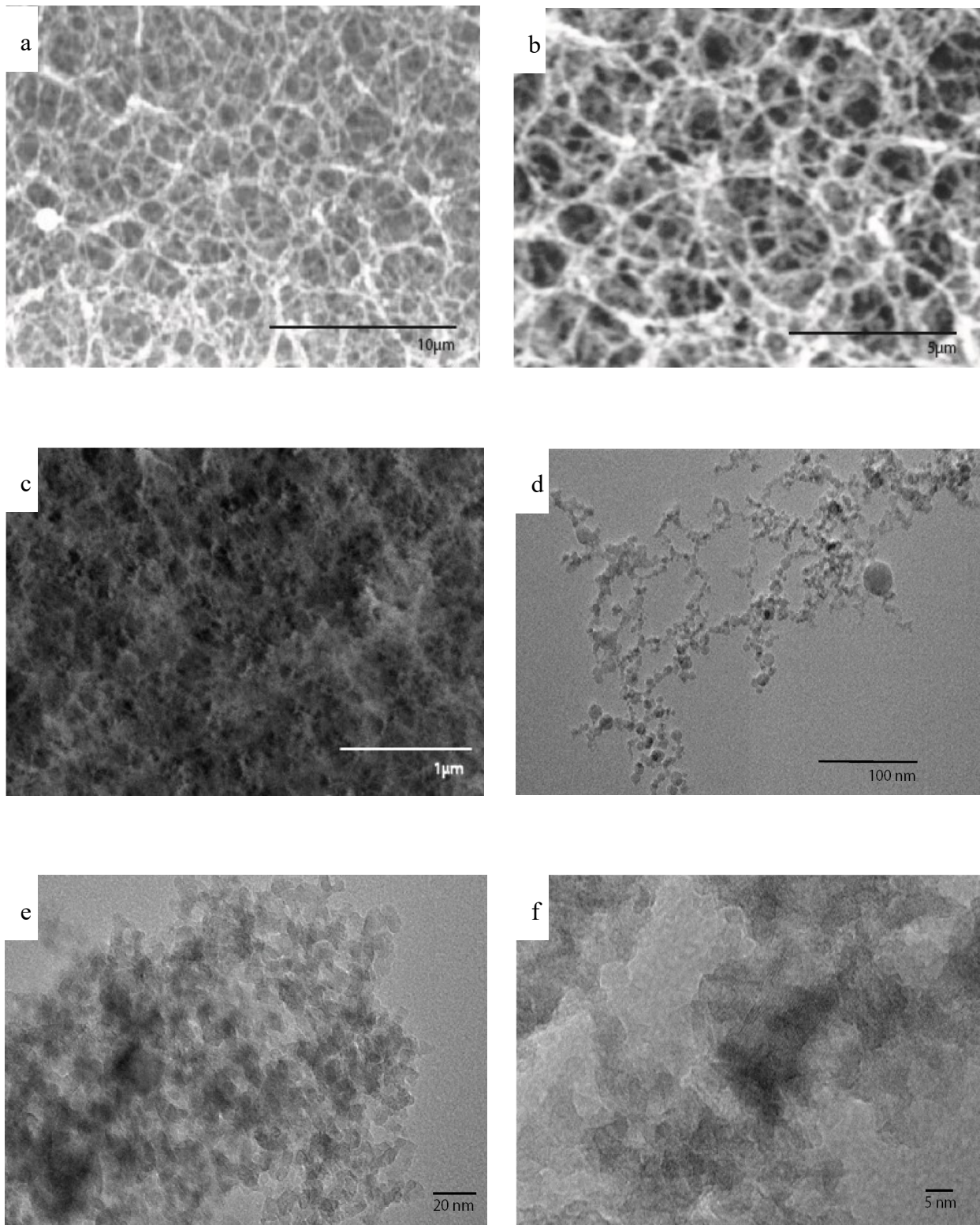


Figure 3.3 a) and b) SEM imaging c) FESEM image (d) –(f) HRTEM images

Figure 3.3 shows a SEM, FESEM and HRTEM images of the interconnected fibrous network of nanoweb structures at varying scales up to 5 nanometers. The size distribution of the nanostructures is given in Figure 3.6 which gives the mean particle size to be around 2 nanometers. The Bohr radius of Aluminum is 1.18 nanometers and it can clearly be seen that the size of the fabricated nanoparticles approach quantum confinement.

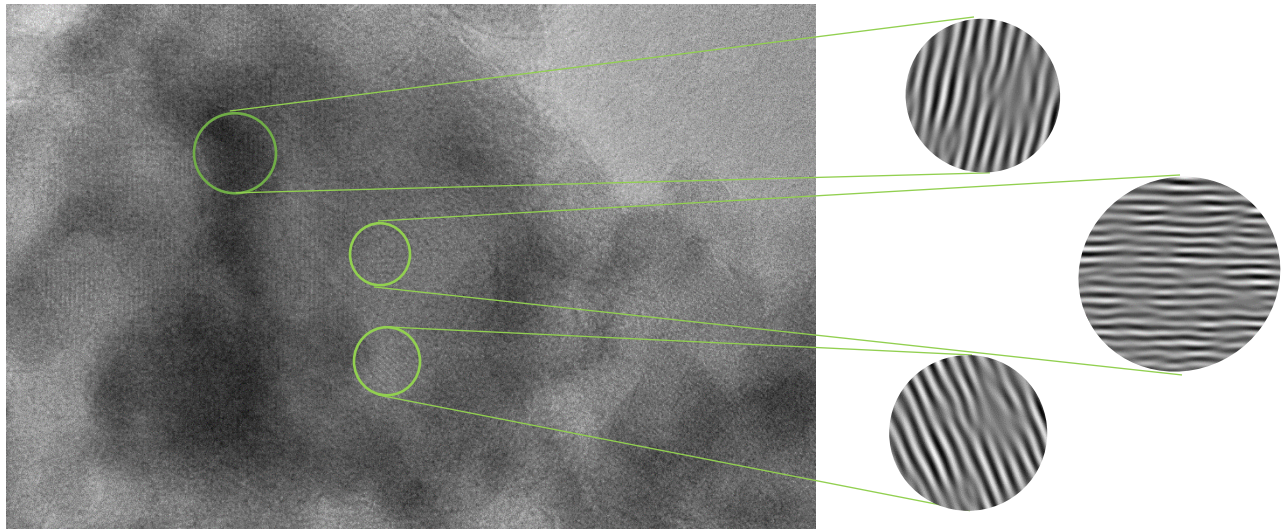


Figure 3.4 HRTEM image showing the d spacing orientation in different planes in the same structure (2MHz).

The HRTEM images reveal the above mentioned multi-crystalline structure of Aluminum nanocrystals. From the HRTEM images in figure 3.6, we can see that there are both a mixture of smooth spherical and multi-edge crystal structure of Aluminum quantum particles. By tuning the laser parameters, we were able to achieve purely spherical and multi-edge particles separately at different conditions. It shows a clear contrast between the smooth spherical nanoparticles and the multi-edge spherical nanoparticles. The above variation was able to be achieved by changing the repetition rate of the pulsed laser system. The lower repetition rate has a high peak power which produces a high ionization temperature and this condition yields a lower cooling time and results in the synthesis of more uneven structures. As the particles have less time to solidify and are repeatedly being irradiated by laser pulse at short durations with a high peak power, they tend to arrange themselves in a more unorganized manner and hence have multiple sharp edges. On the other hand, when a higher repetition rate is employed, this slightly decreases the peak power and increases the cooling time interval for the condensed nanoparticles to agglomerate and so the

nanoparticles take enough time to organize themselves in a more organized manner and hence form a much smooth spherical particle.

HRTEM image in Fig.3.4 shows lattice structure with distortions. The planes oriented in different directions are not smooth and tends to have structural deformations which are due to vacancies in the formed nanostructures. The example of a vacancy is as shown in the Fig. below. Aluminum has a Face Centered Cubic structure (FCC) whereas Alumina has a Hexagonal Crystal Plane (HCP) structure. The Aluminum atom forms the center of the hexagonal plane and fills 2/3 of the crystal plane, connected by Oxygen atoms.

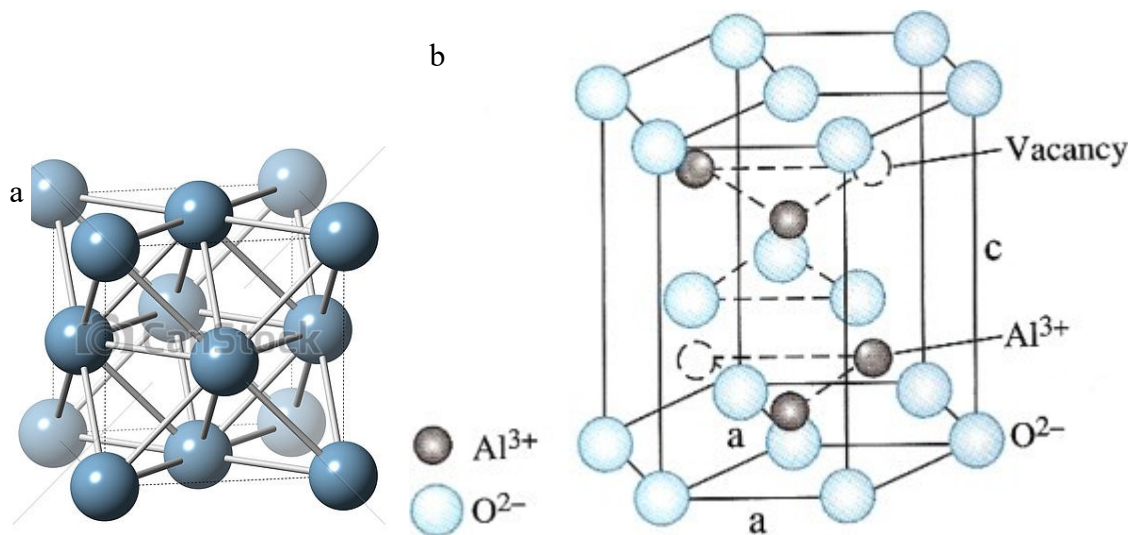
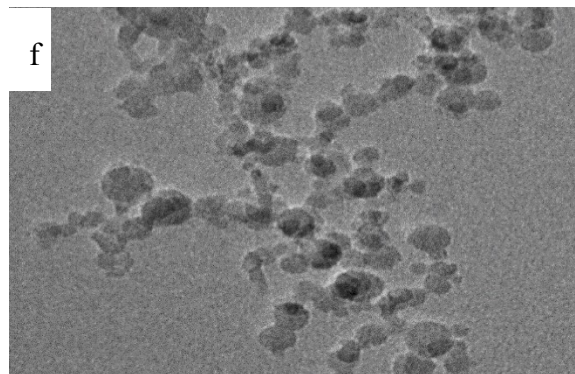
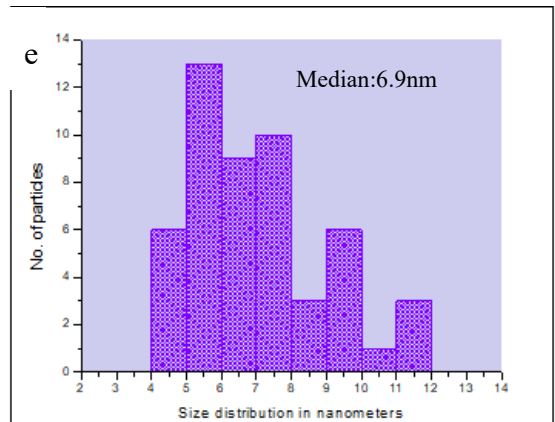
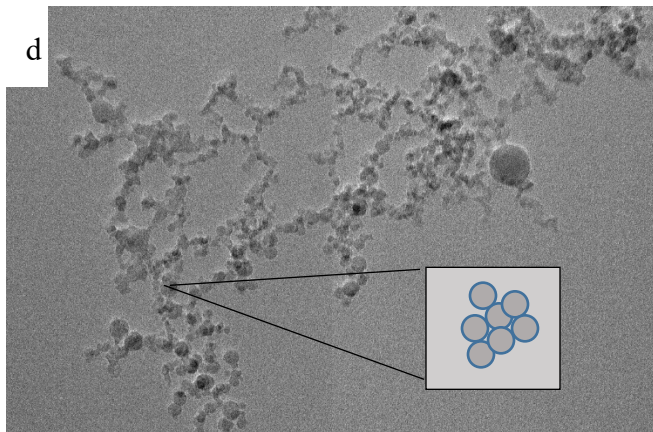
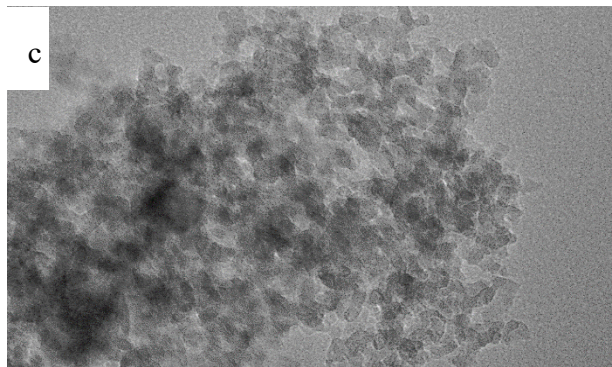
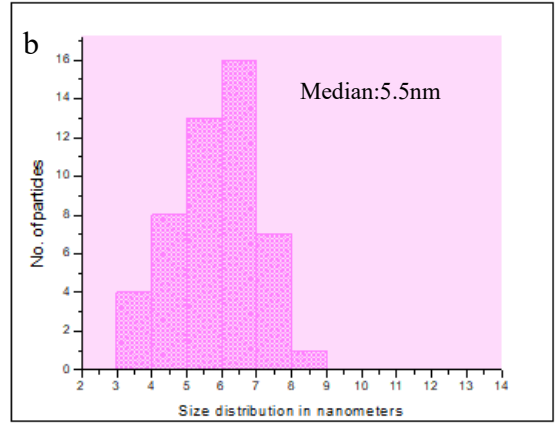
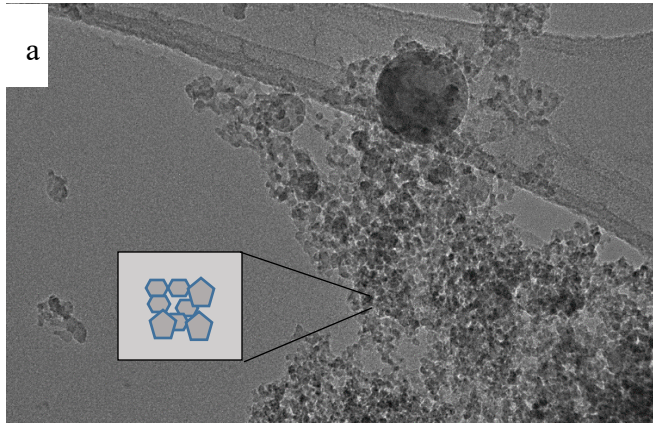


Figure 3.5 a) Cubic crystal structure of Alumina (gamma) b) Hexagonal Crystal Plane structure of Alumina (alpha)

3.2.1 SIZE OF ALUMINUM/ALUMINA NANOSTRUCTURES

Based on the varying ionization energy and the corresponding condensation times, not only the shape but also the size of the structure varies accordingly. At a higher peak power as the cooling time tends to decrease significantly, the nanostructures tend to solidify quickly and hence forms comparatively smaller structures than the particles formed at a low peak power. Also, the substrate was ablated in conditions involving Nitrogen gas (in contrast to the ambient conditions used otherwise) and it showed a mix of both spherical and multifaceted structure with a smaller size than the former two conditions.



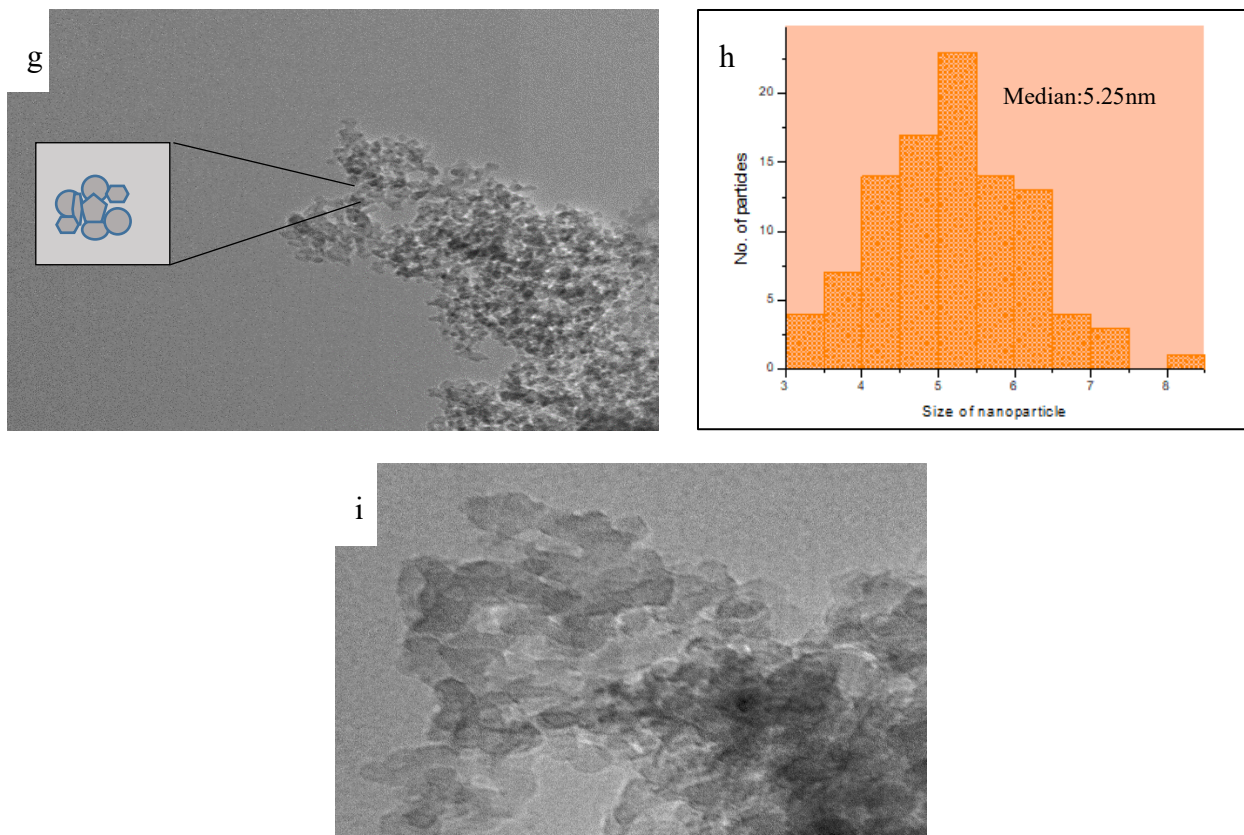
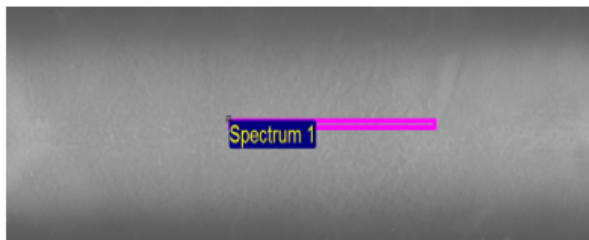
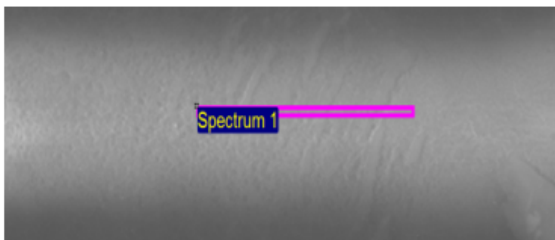


Figure 3.6 TEM images and the corresponding size distribution of nanoparticles for (a-c) multifaceted structures (high peak power) (d-f) spherical structures (low peak power), (g-i) Combination of multifaceted and spherical structures (with Nitrogen gas)

3.2.2 COMPOSITION OF THE NANOSTRUCTURE

Figure 3.7 shows the composition of the fabricated sample which is a mixture of both Aluminum and Aluminum oxide. The higher percentage of Aluminum confirms the presence of both the metal and its oxide. The line EDX mapping on the material and the corresponding percentage of components present in the fabricated material is shown. From the atomic percentage, we can infer that the metal present is 66% which is twice as much as its oxide 33% which indicates that the metal is only partially oxidized thereby confirming our previous statement that both the metal and the metal oxide is present in the fabricated nanostructure. The composition of the metal oxide formed is Al_2O_3 , so the amount of Aluminum required for the oxide is about 22% of the whole sample tested. The remaining percentage of Aluminum present is around 44% of the total which concludes that the amount of metal oxide dominates the presence of Aluminum metal itself. This is also supported by the XPS data which consists of an Al 2p peak at 75 corresponding to

Aluminum in its oxidized state and another peak at 120 corresponding to Al 2s indicating Aluminum metal.



Element	Weight %	Atomic %
Aluminium	54.60	66.97
Oxygen	45.40	33.03

Element	Weight %	Atomic %
Aluminium	54.84	66.83
Oxygen	45.16	33.17

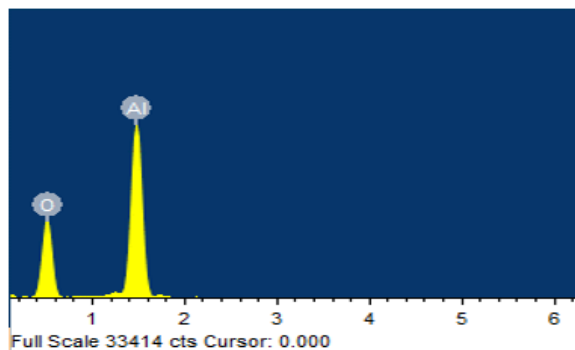
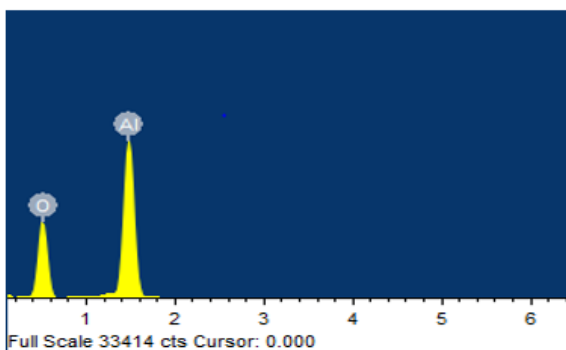


Figure 3.7 EDX for the fabricated sample spherical nanostructures (left) and multifaceted nanostructures (right).

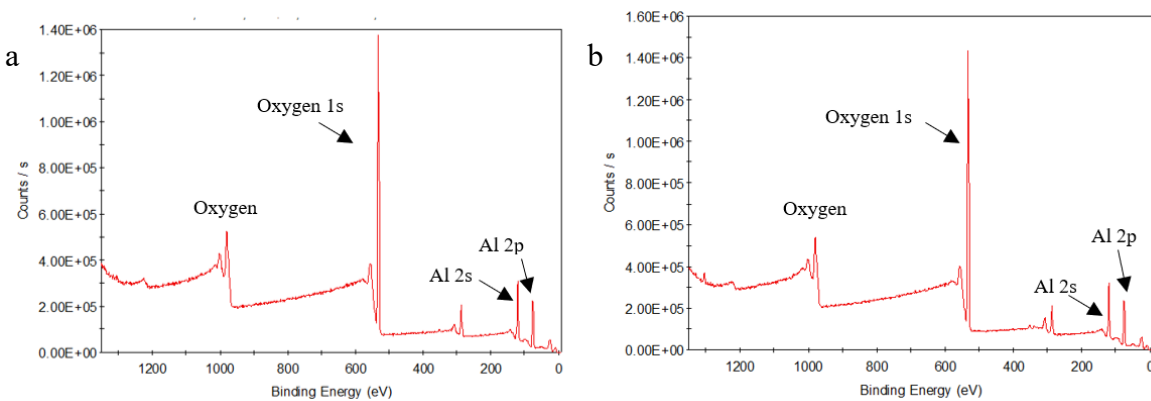


Figure 3.8 XPS data of a) multifaceted nanostructures b) spherical nanostructures

Name	Atomic %	Name	Atomic %
Al2p	28.83	Al2p	29.04
C1s	14.62	C1s	14.27
O1s	55.51	O1s	54.97
N1s	0.4	N1s	0.49
Mg1s	0.64	Mg1s	1.22

Table 3.1 Composition of element present in of a) multifaceted nanostructures b) spherical nanostructures

The XPS data provides the percentage of Aluminum and Oxygen (and any other components, if present) in terms of their binding energy and orbital structures.

The percentage of Aluminum and Oxygen present in each condition gives us an overview of the composition of the Alumina present and the evidence for vacancies. Of the Al₂O₃ structure, the decrease in Aluminum percentage tells us the existence of a vacancy there, refer to Figure 5, in the hexagonal crystal package of Alumina. It can also be used to calculate the thickness of the oxide layer formed around the Aluminum which can be inferred from the relative positioning of the metal oxide peaks and the intensities between the metal and the oxide peaks. With information of the metal:oxide ratio and the area percentage of the metal and its oxide peaks, the actual thickness value of the oxide can be calculated using the equation developed by Strohmeyer and Carlson as follows:

$$d = (\lambda_{ox}) \sin \theta \ln \left(\frac{(N_m \cdot \lambda_m \cdot I_{ox})}{(N_{ox} \cdot \lambda_{ox} \cdot I_m)} + 1 \right) \quad (3.1)$$

where d is the thickness of the oxide film we're trying to calculate, λ_m and λ_{ox} are the Inelastic Mean Free Path of the metal and oxide, N_m and N_{ox} are the volume densities of the metal atoms in the metal and oxide respectively, θ is the take-off angle of the photoelectron.

The peaks in the above XPS graph has the different phases of Alumina peaks overlapped and were then fitted using Origin pro 8 multiple peak fitting option after which the above required values were calculated and the analysis was carried out which resulted in an oxide layer of 1.47nm and

1.46nm thick for the spherical and multifaceted structures, hence not showing a big difference between oxidation of the two elements. This value of the oxide layer obtained is in agreement with the calculated value from the TEM images (Refer Figure 3.10).

3.2.3 LATTICE SPACING OF ALUMINUM/ALUMINA

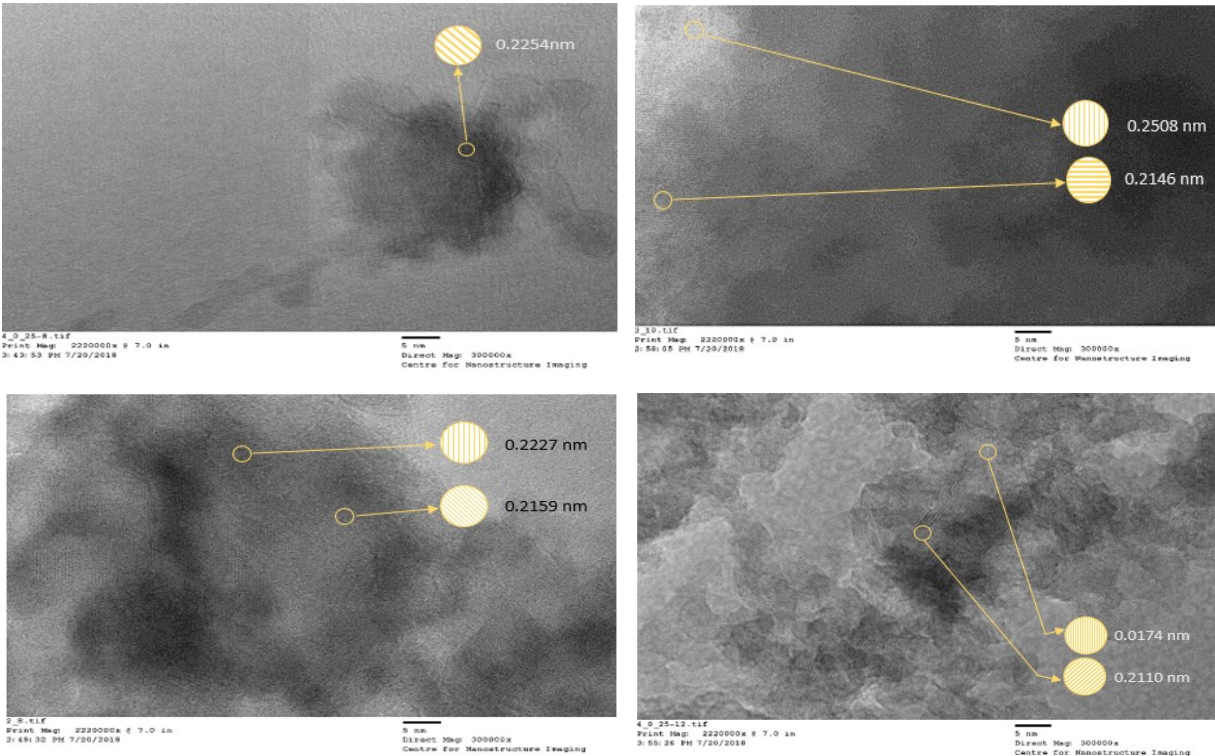


Figure 3.9 Lattice spacing values calculated for various crystal orientation (HRTEM images) for multifaceted nanostructures

The lattice spacing images provides data to prove the presence of crystalline structure, thereby confirming the presence of Alumina and Aluminum (Refer Table 1). Lattice spacing or ‘d’ spacing is referred to as the distance between two adjacent unit cells in a molecule.

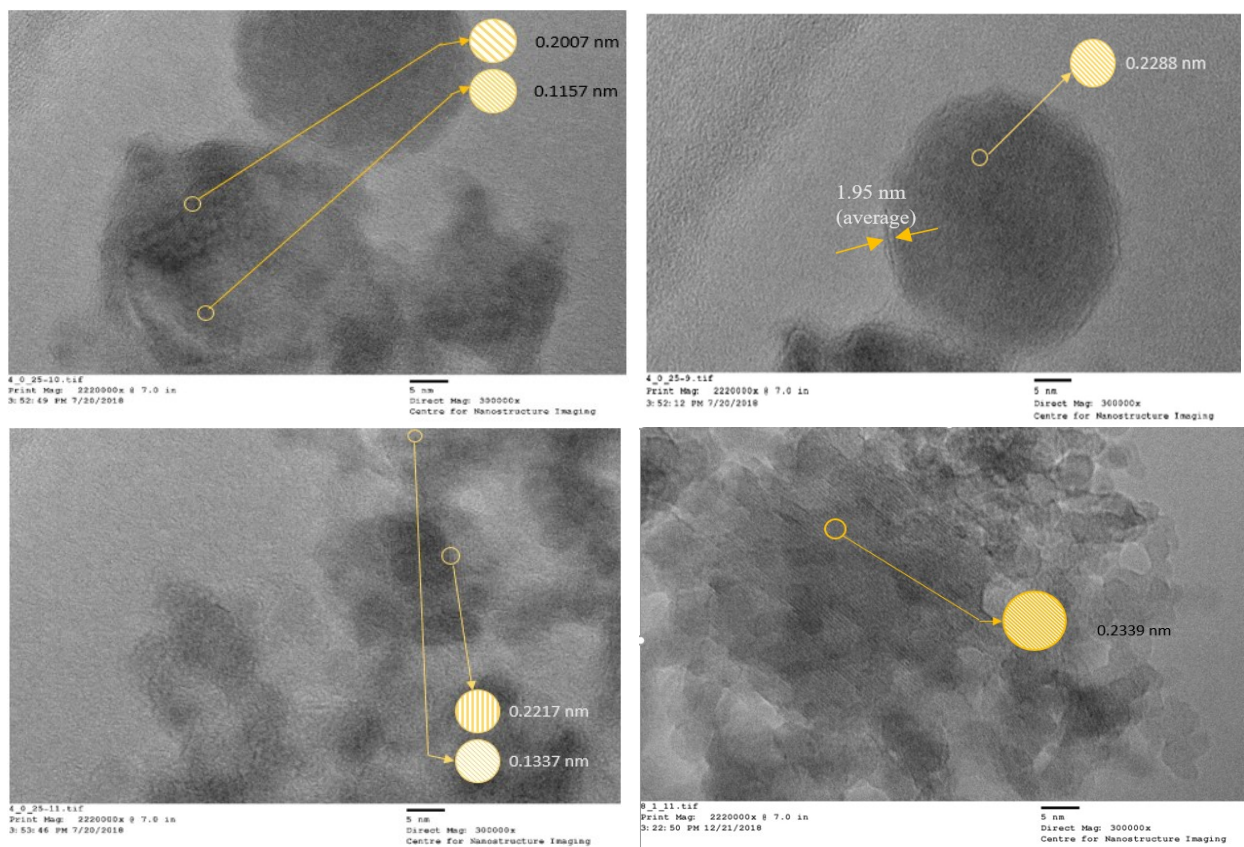


Figure 3.10 Lattice spacing values calculated for various crystal orientation (HRTEM images) for spherical nanostructures

d-spacing (in Å)	Aluminum (hkl plane)	Aluminum oxide (hkl plane)
1.1565	222	
1.3365	220	
2.0283	200	
2.1104		113
2.2159		115
2.2642		111
2.5075		104

Table 3.1 d-spacing for Aluminum/Aluminum oxide and the corresponding planes

The SAED proves the co-occurrence of crystalline and amorphous alumina, as shown in Figure below. The presence of rings shows the amorphous phase of the nanoparticle and the presence of dots represent the crystalline phase.



Figure 3.12 SAED pattern showing a crystalline-amorphous structure

Here, the dots in a ring pattern explain the coexistence of amorphous and crystalline phases in the fabricated material. Figure below represents SAED pattern taken at 3 different points on a sample nanostructure, revealing that one point is more crystalline another being highly amorphous and one being a mixture of both phases.

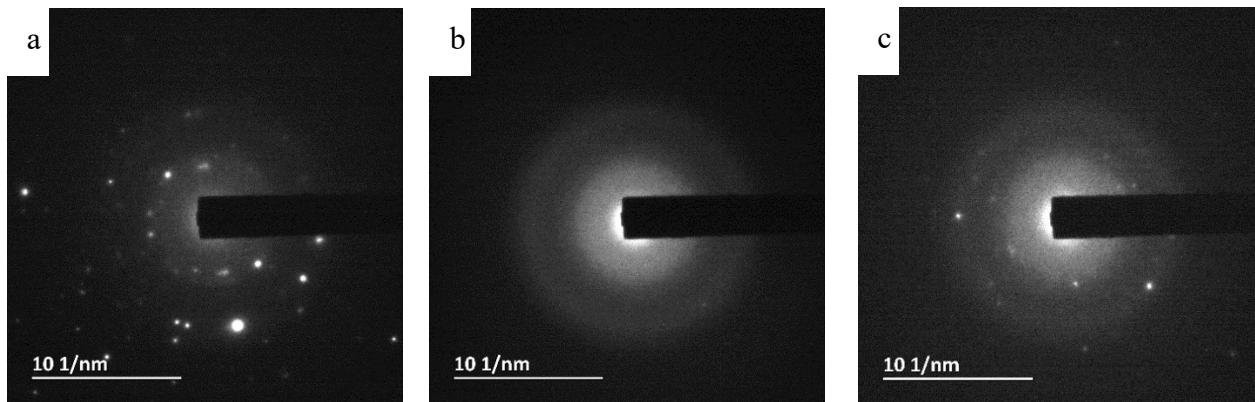


Figure 3.13 SAED showing a) crystalline b) amorphous and c) crystalline-amorphous phase coexistence on the same sample at different points

3.3 OPTICAL PROPERTIES OF ALUMINUM/ALUMINUM OXIDE

With the aim of obtaining the optical band gap of the fabricated Aluminum/Alumina nanoparticles, the UV-vis absorption spectroscopy was performed shown in Figure. There are two prominent absorption peaks obtained corresponding to λ at 210 and 250, representing the absorption wavelength of Alumina and Aluminum respectively. This provides evidence that both Aluminum and oxides of Aluminum are present in the sample. (a point in XRD and line edx).

A Tauc plot was plotted based on the method proposed by Wood and Tauc using the values from the absorption spectra obtained. Calculations were performed based on the equation

$$(h \alpha \nu) \propto (h \nu - E_g)^n \quad (3.2)$$

where α is the absorbance, h is the Planck's constant, ν is the frequency, E_g is the optical energy band gap and n is a constant corresponding to the various electronic transitions ($n=1/2, 2, 3/2$ or 3 for the band gap of the fabricated material was found to be 5.5eV which corresponds to alpha phase of Alumina).

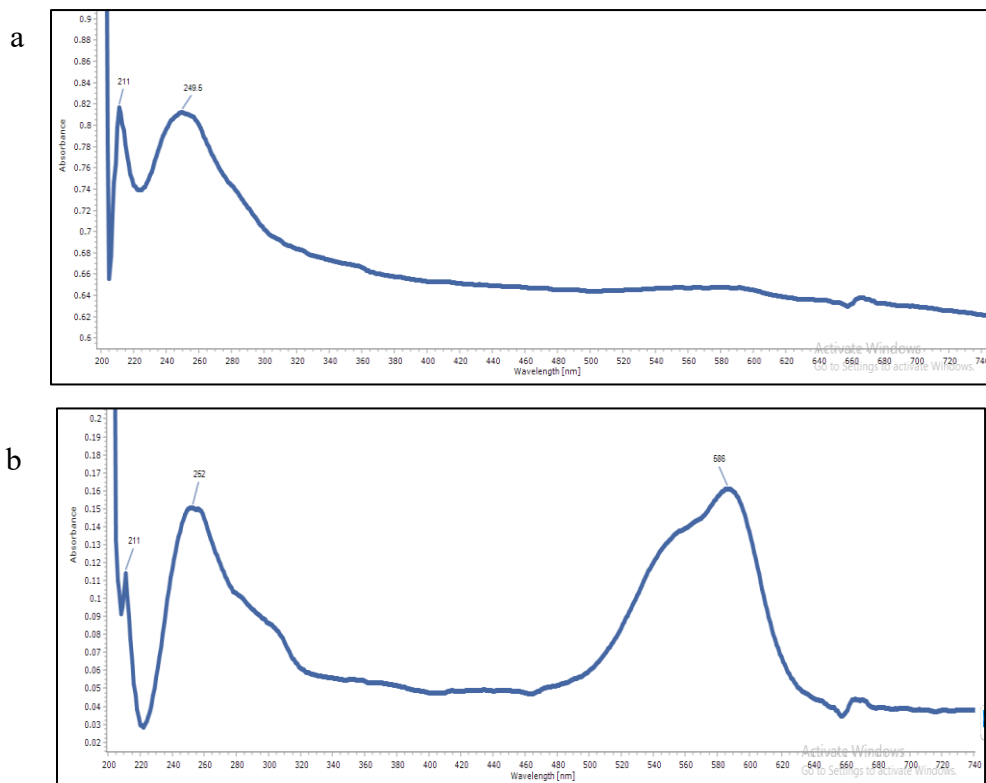


Figure 3.14 UV-Vis spectrum of Aluminum/Alumina a) in ethanol b) in ethanol with CV

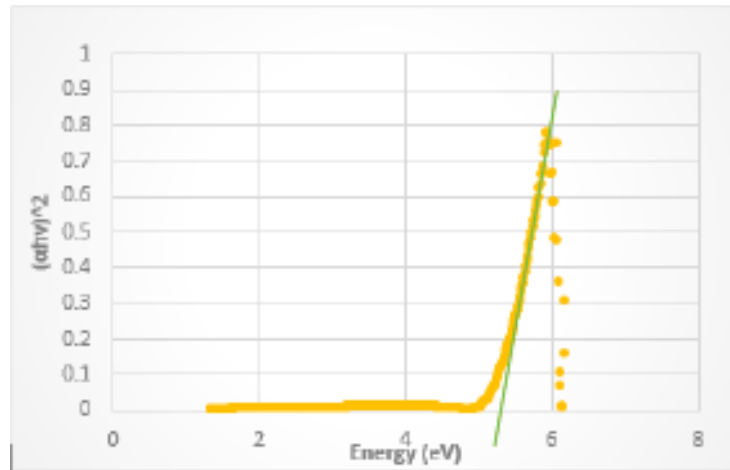


Figure 3.15 Tauc plot to determine the band gap

The Tauc plot proposed by *Tauc*, is derived from the absorption spectrum (Figure 3.14a) and it provides the band gap value for the fabricated Aluminum/Aluminum oxide nanostructure. The band gap value obtained from the Figure 3.15 is 5.5eV and it lies within the range of Alumina.

3.3.1 RAMAN SPECTRUM OF ALUMINUM/ALUMINA

The Raman spectrum of the Aluminum/Alumina nanostructures fabricated are as shown below, in comparison with the Aluminum substrate. The enhancement seems to be greater for the multifaceted nanostructure in comparison with the spherical nanostructures fabricated, owing to their sharp-edged corners which acts as tips for Tip Enhanced Raman Spectroscopy in addition to their roughened surfaces for SERS.

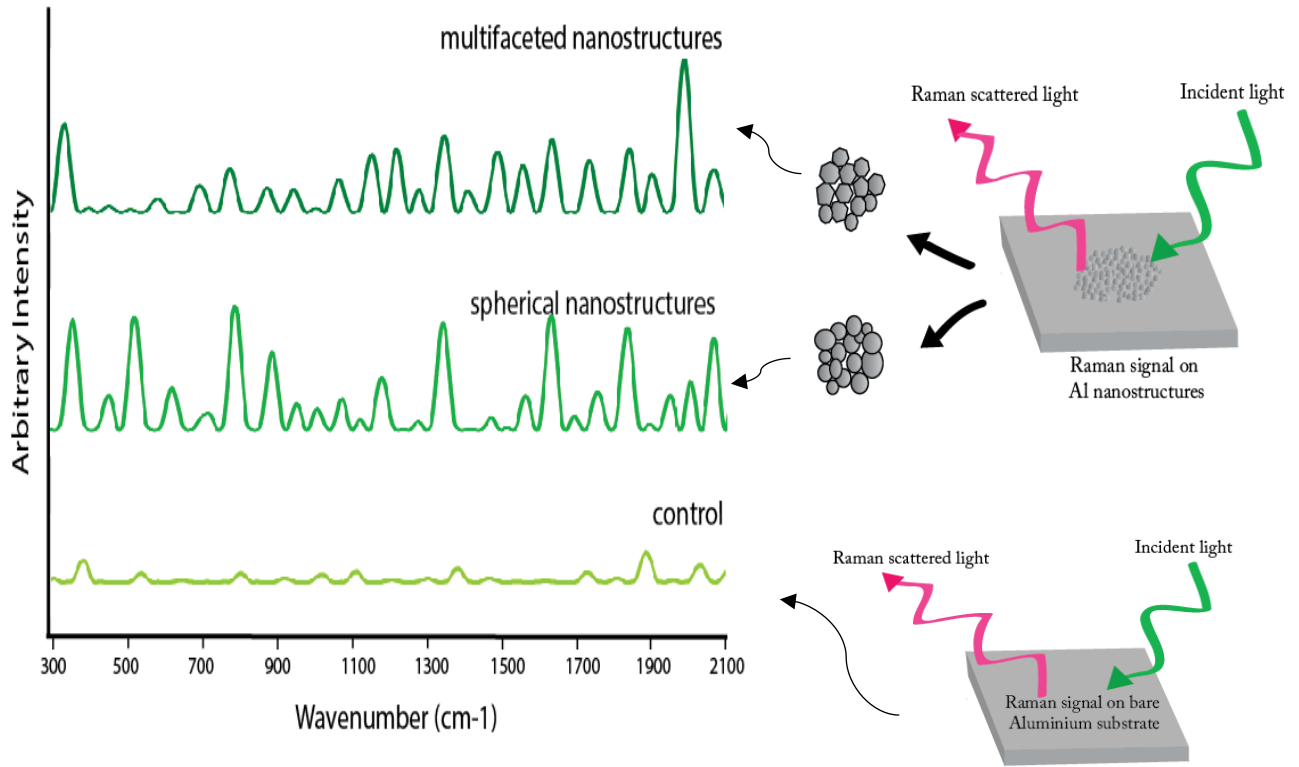


Figure 3.16 Raman spectra of bare Aluminum substrate and nanofabricated substrate (multifaceted and spherical nanostructures)

The detailed peak structure of the Aluminum nanostructures fabricated at 2 different laser conditions is given in the figure below:

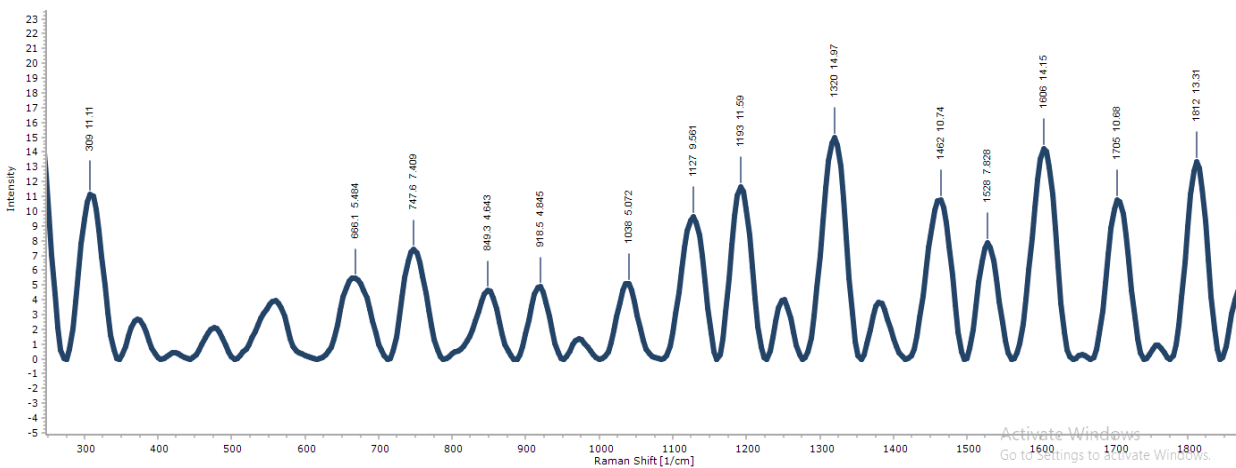


Figure 3.17 Raman spectrum for sample fabricated at a higher ionization energy (multifaceted nanostructures)

The Raman spectra of the Aluminum/Aluminum oxide nanostructures are shown in Figures 3.17 and 3.18. In figure 3.17, the peaks at 234(235), 485(485), 739(747), 847(833) and 1608(1600) are that of Aluminum and the ones at 739(745), 571(567), 531(534) are attributed to the Aluminum oxide as per literature.

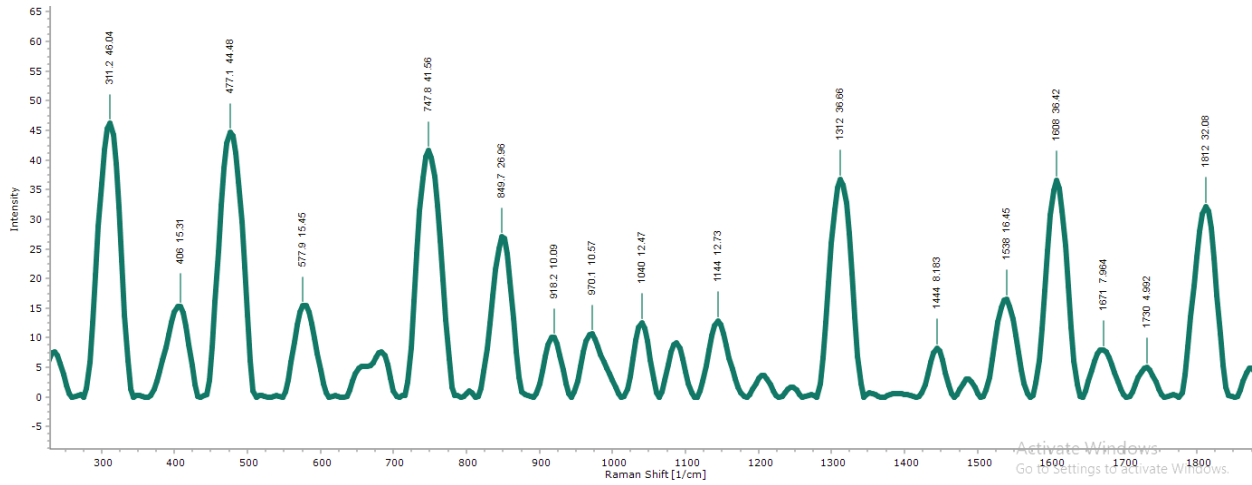


Figure 3.18 Raman spectrum for sample fabricated at a lower ionization energy (spherical nanostructures)

In figure 3.18, the peaks at 234(235), 475(477) 745(747), 967(955), 1143(1141), 1300(1312) and 1608(1600) are that of Aluminum and the ones at 388(385), 686(674), 745(745) are attributed to the Aluminum oxide.

The shift in peaks in the Raman spectra provides information on the stresses present within the fabricated nanostructures. By determining the shift in the observed peaks on the fabricated substrate with respect to the peaks on the bare substrate (Refer figure 3.16) the residual stress in the fabricated structure can be calculated using the following formula:

$$\sigma(MPa) = \sigma_{s(Al)} \times (\omega - \omega_0)$$

Where σ is the residual stress, ω_0 is the peak position of the bare substrate and ω is the shifted peak position in the nanostructures spectra $\sigma_{s(Al)}$ is the stress sensitivity of Aluminum. These stresses can be either tensile or compressive based on the shift in the observed peak of fabricated structure being towards the left or right respectively thereby creating a positive or negative peak position. Our calculations show that both tensile and compressive stresses exist in the material.

For example, the peak at 485cm^{-1} is shifted to the left, indicating the presence of a tensile stress on the material, the value of which can be calculated using the formula above.

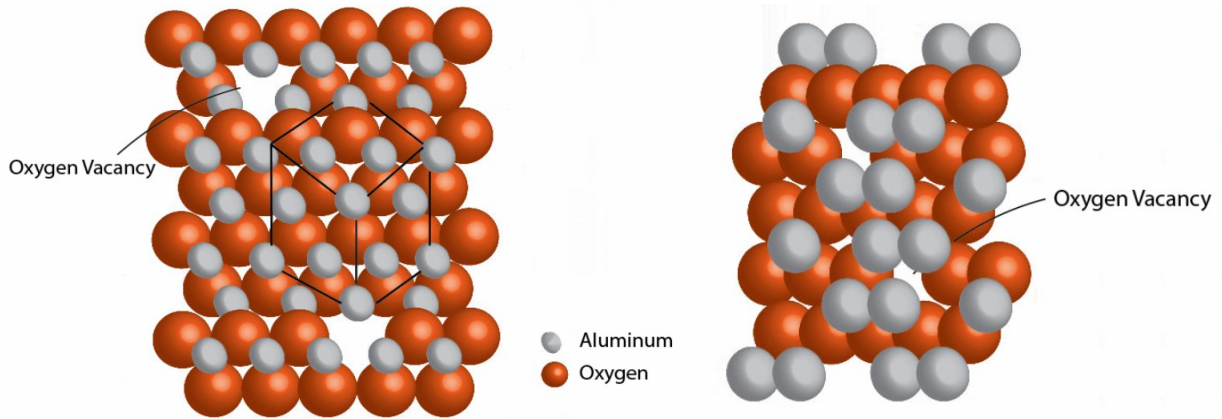


Figure 3.19 Crystal structure of Alumina a) gamma phase b) alpha phase with Oxygen vacancies based on experimental data

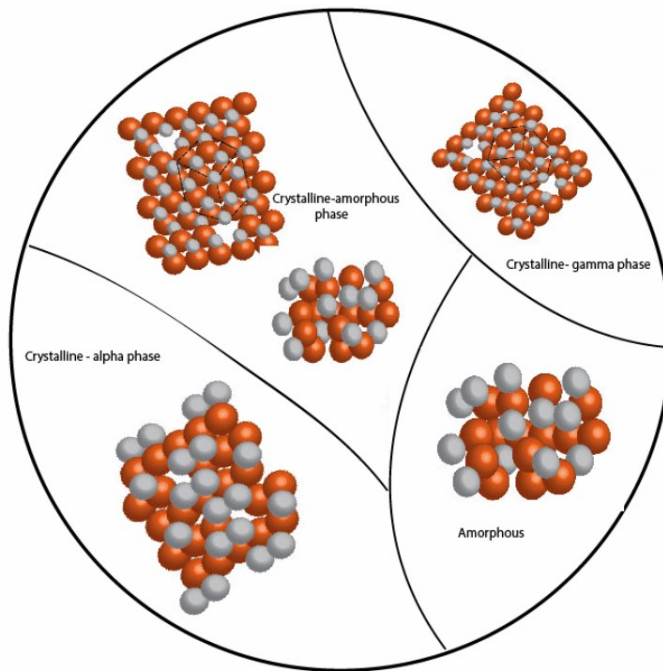


Figure 3.20 Multi-crystalline-amorphous grain structure of Alumina

The above figure represents the various grain boundaries enclosing different crystal structures and amorphous structures of fabricated nanoparticles showing their coexistence.

3.4 SUMMARY

A novel 3-dimensional Aluminum based nanostructure was synthesized using ultrashort pulsed laser with tunable parameters. The modification of laser parameters helped in fabricating our nanostructures with desired properties pertaining to future applications.

The new Al based nano material was characterized using SEM, HRTEM, FESEM, UV-Vis Spectroscopy, Raman spectroscopy, XPS and EDX. SEM, FESEM and TEM were used to define the geometrical features of the particle whereas the optical properties were defined by UV-Vis and Raman spectroscopy. XPS and EDX gave data on the composition of the fabricated nanostructure with respect to its oxide layer and the phases of Alumina formed.

Three unique shaped nanostructures were defined- spherical nanostructures, multifaceted nanostructures and spherical- multifaceted nanostructures. The percentage composition of Aluminum and Oxygen obtained from XPS and EDX revealed the existence of both Alumina and Aluminum metal nanostructures which was also supported by the UV-Vis spectrum in Figure 3.13. Also, the band gap calculated was inclined more towards Alumina which combined with the above results also showed the existence of oxygen vacancies in the structure as shown in Figure 3.18. The calculation of d-spacing also provided supporting data towards the existence of the metal and its oxide with a multi-crystalline structure. The SAED pattern too shows the coexistence of crystalline and amorphous phase in the material forming multi-crystalline-amorphous boundary grain structure as shown in Figure 3.19.

The Raman signals were analysed to find the shift in the peaks and to analyze the corresponding stresses acting on the material. A final image is rendered based on the data referred to from literature with respect to the experimental results obtained from the characterization experiments performed.

CHAPTER 4 BIO-MOLECULAR DETECTION

4.1 INTRODUCTION

This chapter demonstrates the Enhanced Raman Scattering effect of the fabricated nanostructures by testing it with molecular dyes, biomolecule and a cancer biomarker. The dyes namely CV and R6G are some of the common dyes used to test the enhanced Raman sensing ability of a material. The biomolecule is used to prove that the fabricated nanoparticle can detect biological markers in our body and its sensitivity towards them. The cancer biomarker sensing provides substantial evidence to apply Aluminum/Alumina nanoparticles for cancer detection using cells.

Molecular dyes such as CV and R6G were physically adsorbed on the nanoparticles rough surface area and Raman spectrum of the same at multiple wavelength provided varying enhancement factors up-to picomolar concentration. The SERS is mainly due to charge transfer mechanism, owing to an enhancement factor value of the order of 10^4 , and the Photon Induced Charge Transfer mechanism can be explained with reference to the UV-Vis spectrum (Refer Fig.6).

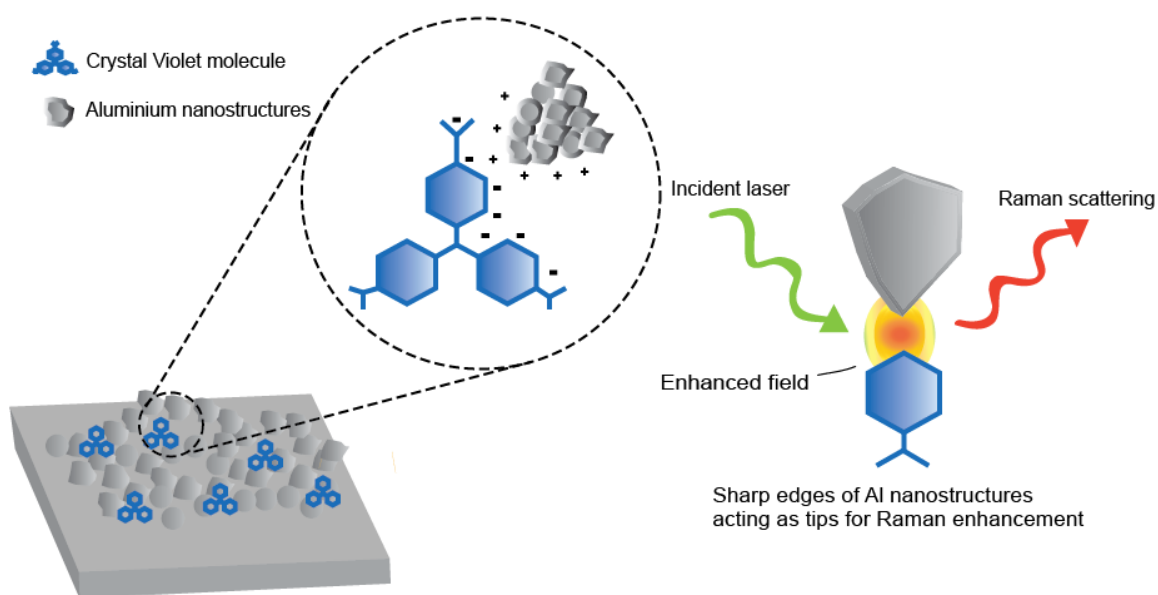


Figure 4.1 Electromagnetic enhancement mechanism of Aluminum nanostructures by Tip enhanced Raman Spectroscopy

A part of the enhancement also takes place due to electromagnetic enhancement due to Aluminum metal nanoparticles present, the mechanism of which is given in figure below. Alumina, being a dielectric has a bandgap which separates its valence band and conduction band electrons, which interacts with the dye molecules and when induced by a photon of a particular wavelength, charge transfer occurs between the corresponding bands of the dye molecule and the Alumina nanostructures.

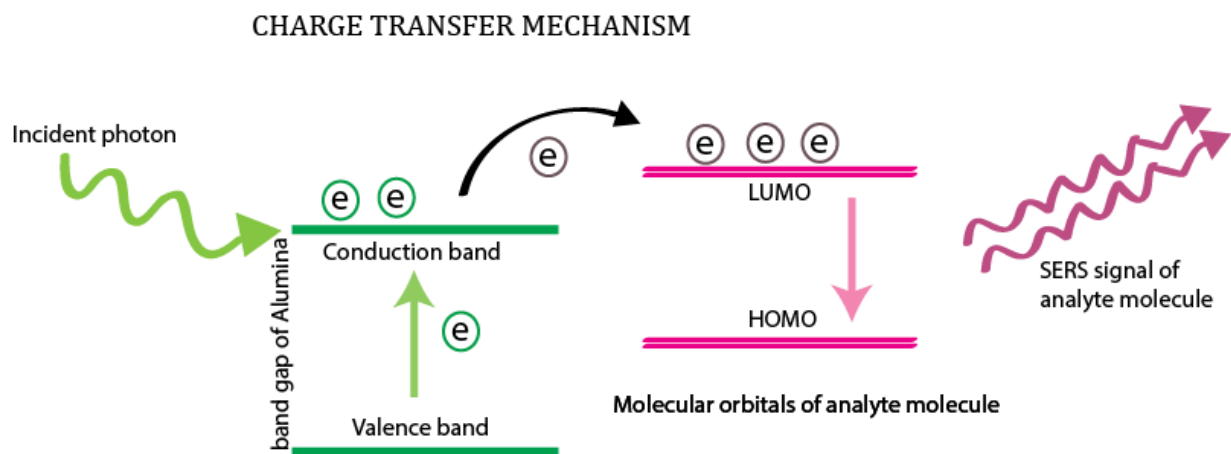


Figure 4.2 Charge transfer mechanism induced by the incident photon, electrons transferred to molecular orbitals of analyte molecules

In addition to the two molecular dyes, which by themselves substantiate enough evidence for biosensing, we also test the material with two biomolecules namely cysteine and Carcino-Embryonic Antigen (CEA) to further prove the credibility of the nanomaterial fabricated.

The experiment was carried out by dropping a 10 microliter of the dye/biomolecule solution over the nanostructures and the spectrum was taken at the wet condition as well as the dry condition. Results show that wet condition provides better results in compared to the air-dried samples, so further analysis was carried out at wet condition. Experiments were done on both the multifacteted and spherical nanostructures at 2 different wavelengths, 532nm and 785nm, at millimolar, micromolar, nanomolar, picomolar and femtomolar for the molecular dyes and up to nanomolar for cysteine and at micromolar for CEA. The Enhancement Factor was then carried out using the following equation:

$$\text{Enhancement Factor} = \frac{I_{SERS} * N_{native}}{I_{native} * N_{SERS}} \quad (4.1)$$

Where I_{SERS} and I_{native} are the respective intensities of the chosen characteristic peaks of Raman spectra corresponding to the analytes adsorbed on the nanostructures and bare substrate. N_{native} and N_{SERS} are the number of molecules adsorbed on the surface and is calculated using the concentration, density and atomic weight of the analyte molecule, and the focal depth of the Raman laser beam.

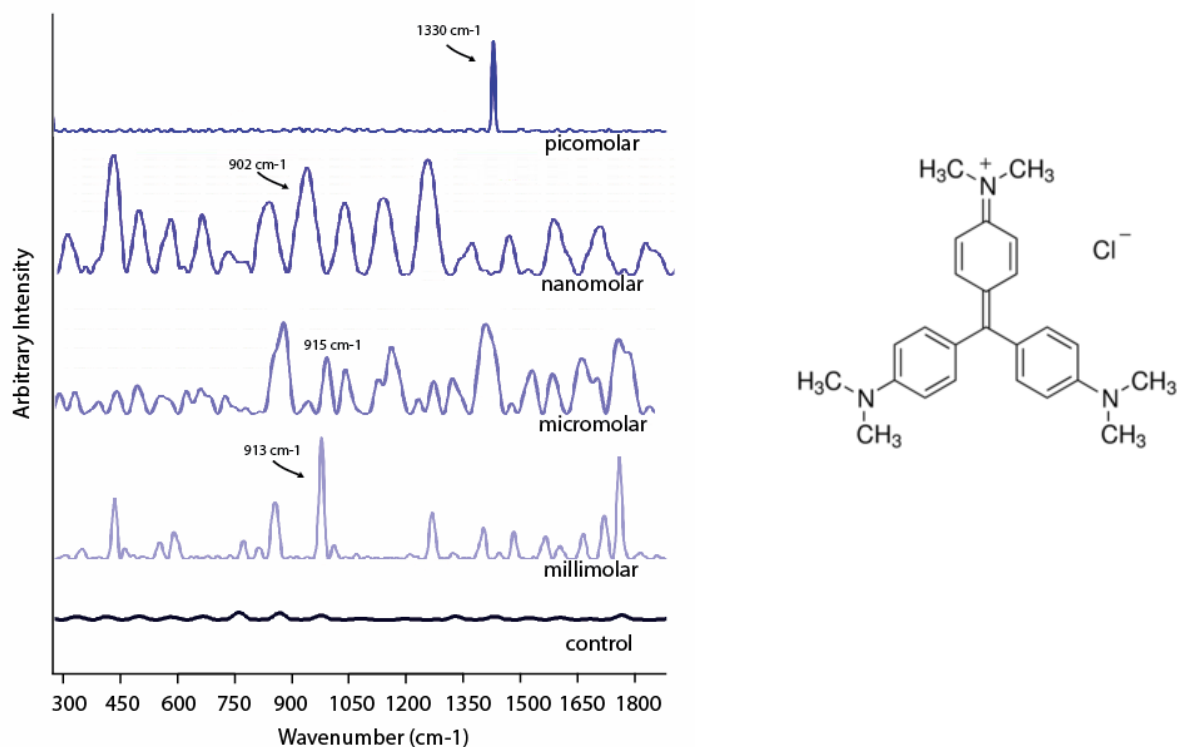


Figure 4.3 Raman spectra of CV adsorbed on Al nanostructure at 532nm wavelength on multifaceted nanostructure

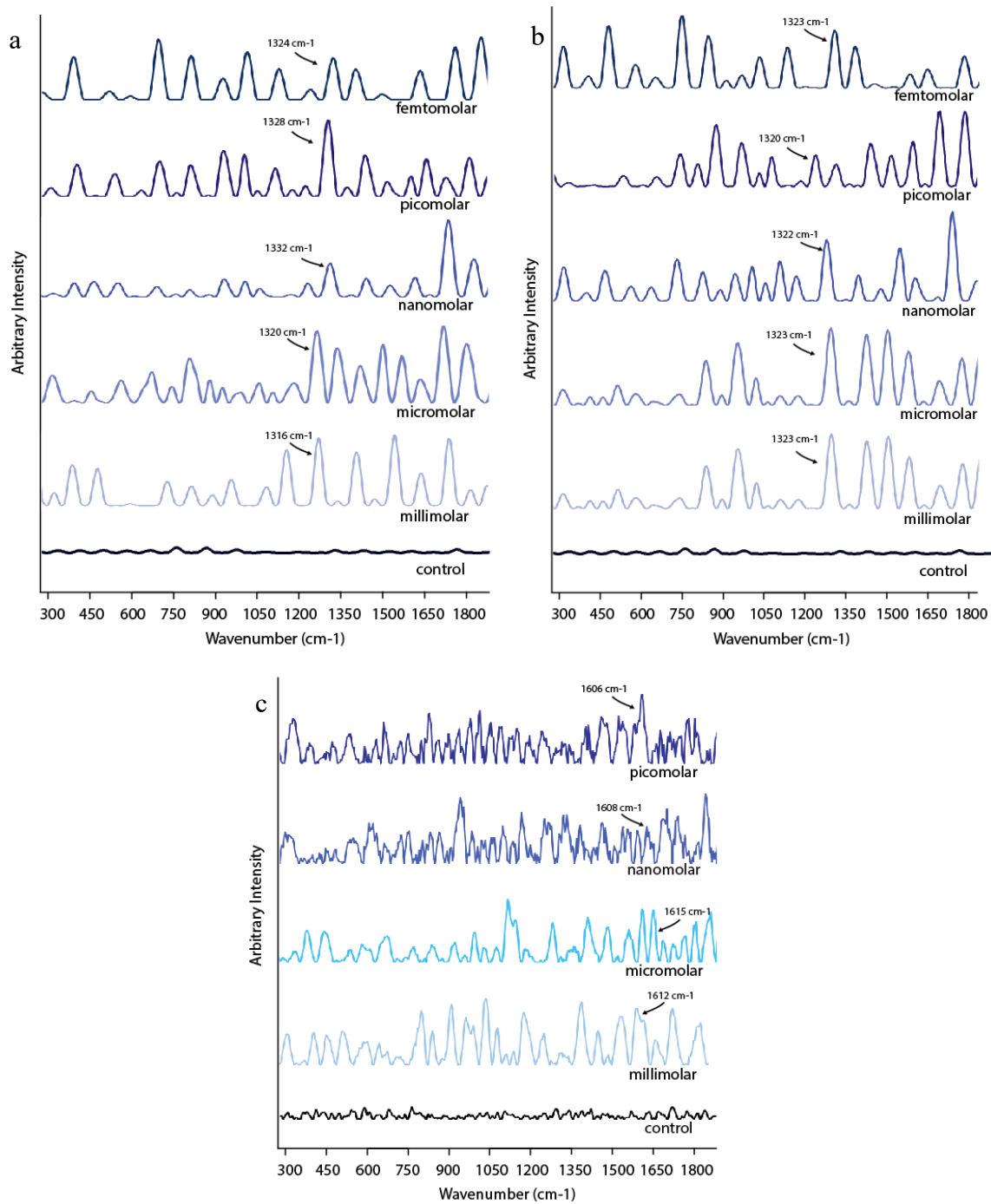


Figure 4.4 Raman spectra of CV adsorbed on Al nanostructure at 785nm wavelength on a) multifaceted nanostructure, b) spherical nanostructure c) spherical-multifaceted nanostructure

Raman peaks for Crystal Violet (from references)	Raman peaks for Crystal Violet (observed)	Assignment of peaks
416	422	Out-of-plane bending mode of C-C _{center} -C
521	530	Bending mode of C-N-C
557	561	Out-of-plane aromatic C-C deformation
722	730	C-N-C symmetric stretching vibration
913	914	C-H out of plane bending modes
1169	1176	C-H in-plane bending mode
1357	1371	Stretching vibration of nitrogen and phenyl ring.
1579	1585	In-plane aromatic C-C
1614	1622	In-plane aromatic C-C

Table 4.1 Observed peaks of Crystal Violet with peak assignments from literature

The enhancement factor for CV adsorbed on the nano probes are calculated using equation (3) with the peak intensities at 1357 peak red shifted to varying values at different concentration. Owing to the value of Enhancement factor obtained, the mechanism of SERS involved in the process can be attributed to both charge transfer and plasmonic resonance, charge transfer playing the major role as it is a dielectric material and is proven using UV-Vis spectrum obtained earlier.

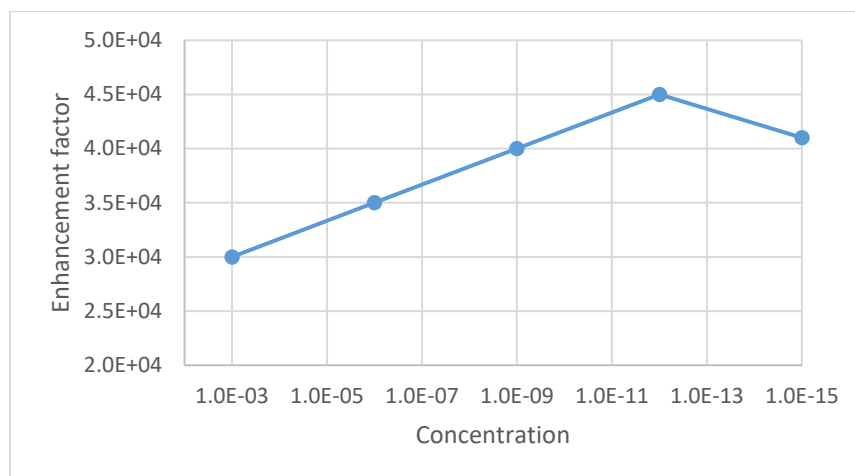
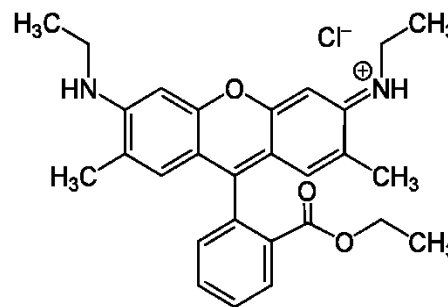
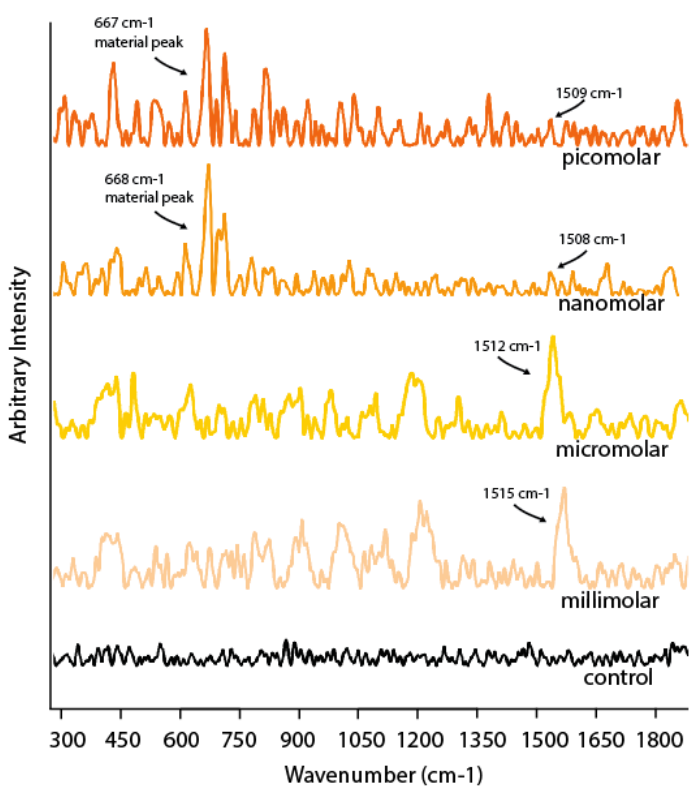


Figure 4.5 Enhancement factor with varying concentration for CV adsorbed on multifaceted nanostructures



Rhodamine6G

Figure 4.6 Raman spectra of R6G adsorbed on Al nanostructure at 532nm wavelength on multifaceted nanostructure

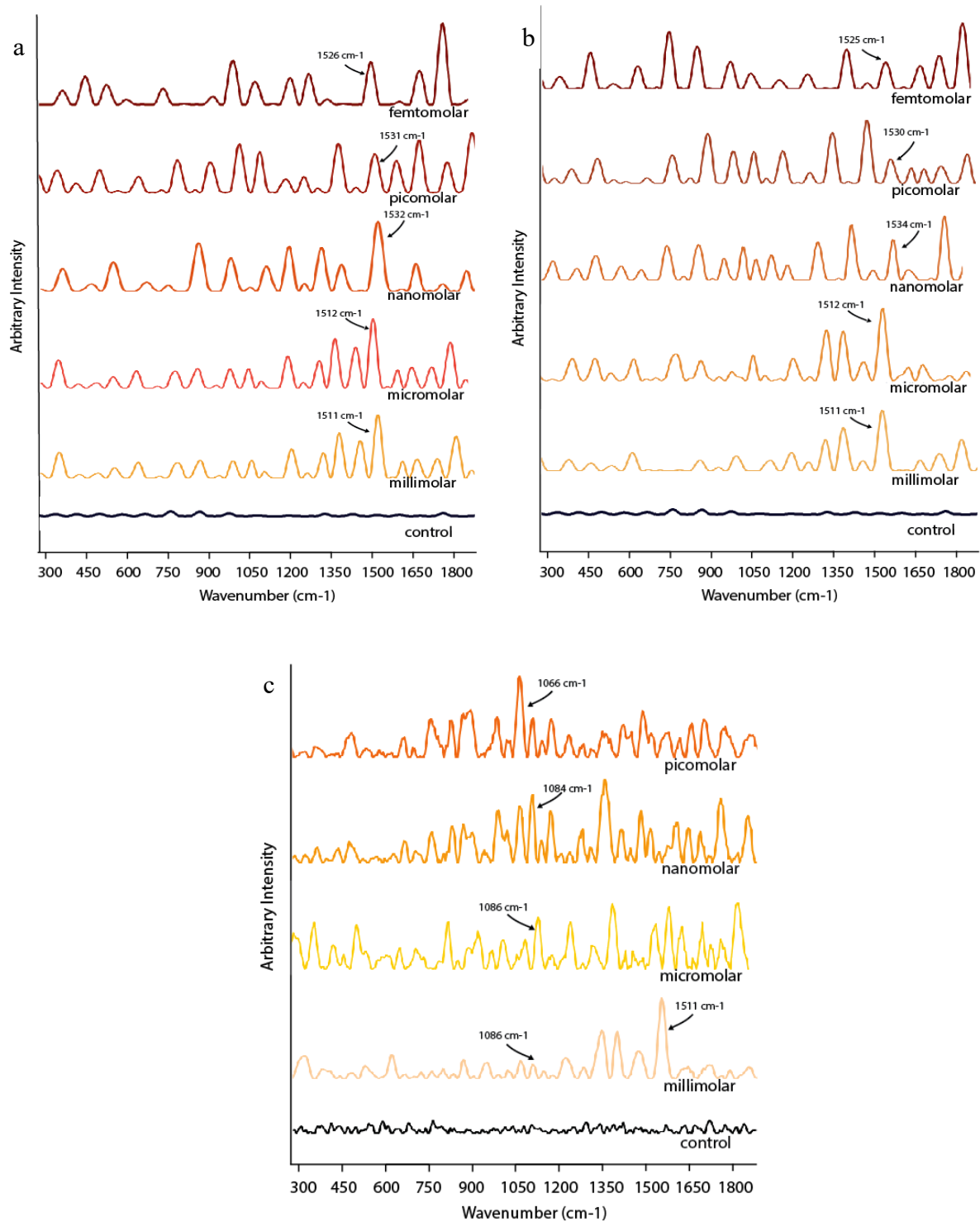


Figure 4.7 Raman spectra of R6G adsorbed on Al nanostructure at 785 nm wavelength on
 a) multifaceted nanostructure b) spherical nanostructures c) spherical-multifaceted
 nanostructure

R6G peaks from references	R6G peaks observed	Peak Assignment
611	612	C-C-C ring isotropic bending
773	774	C-C-C ring isotropic bending
1086	1081	Beta(CH)
1127	1126	C-H stretching
1183	1189	C-H isotropic bend
1310	1311	C-O-C stretching
1360	1366	Aromatic C-C stretching
1508	1511	Aromatic C-C stretching
1573	1571	Aromatic C-C stretching
1648	1653	Aromatic C-C stretching

Table 4.2 Observed peaks of Rhodamine 6 G with peak assignments from literature cm^{-1}

The enhancement factor for Rhodamine 6G adsorbed on the nano probes are calculated using equation (3) with the peak intensities at 1511 for the multifaceted and spherical nanoprobes and at 1086 for the spherical-multifaceted probes. As the peak is slightly shifted in all three conditions, the shifted values are used for the calculation.

The EF values are then compared for the femtomolar concentration for the three types of nanostructures fabricated and is given in Figure 4.9. It is seen that the multifaceted structures provide the highest enhancement value, owing to its sharp corners which undergo Tip Enhancement as shown in Figure 4.9.

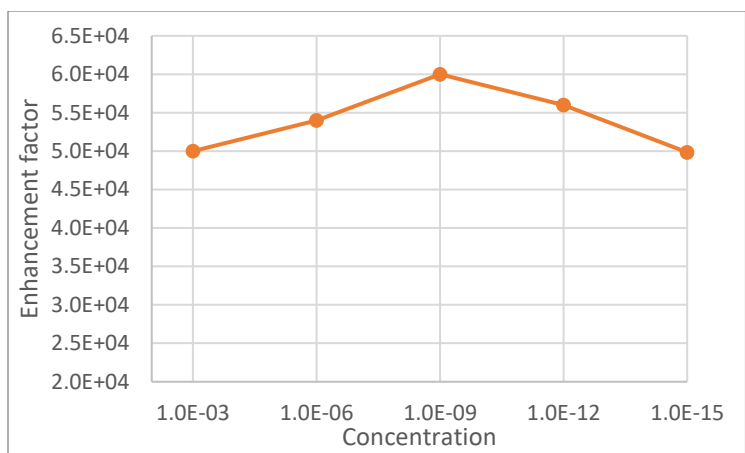


Figure 4.8 Enhancement factor with varying concentration for R6G adsorbed on multifaceted nanostructures

Additional biomolecule detection testing was carried out for the fabricated nanostructures using the biomolecule cysteine in order to determine its potential as a universal SERS nanoprobe. The particular biomolecule was chosen owing to the increase in its levels during certain diseases such as cardiovascular disorders and neurological toxicity which makes it a disease signalling biomarker in our body.

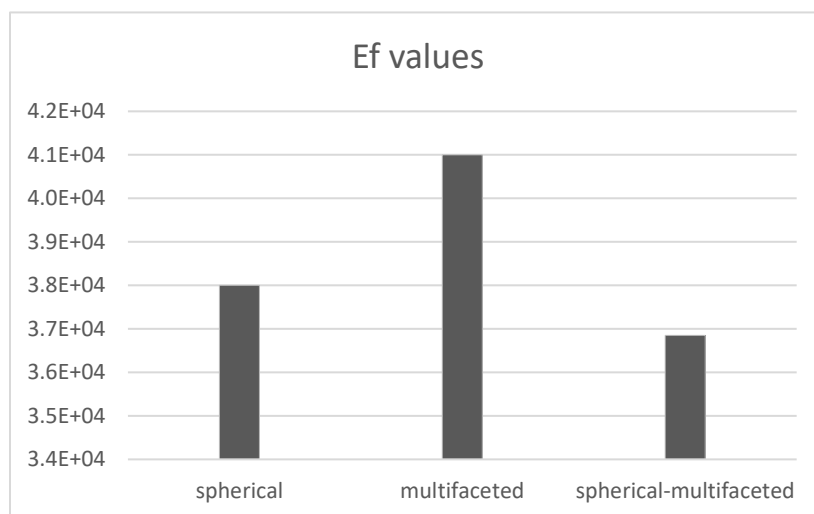


Figure 4.9 EF values comparison for different morphology of nanostructures

Cysteine possess a highly reactive sulfhydryl group in its side chain (shown in Figure 4.10) which makes its affinity to the oxide layer easier. Also, it is said to have a low Raman cross-section which decreases the ease of detecting them using SERS technique. The ability of our nanostructures to detect the molecule becomes challenging owing to this property and therefore it can be said to be highly sensitive to biomolecules.

Cysteine peaks from references	Cysteine peaks observed	Peak Assignment
638	627	CS stretching
798	797	CCC symmetrical stretching
905	926	C-COO- stretching
1100	1111	C α -N stretching
1197	1228	CH ₂ twisting
1324	1312	C α H bending
1406	1416	COO- stretching
1426	1429	CH ₂ bending

Table 4.3 Observed peaks of Cysteine with peak assignments from literature cm⁻¹

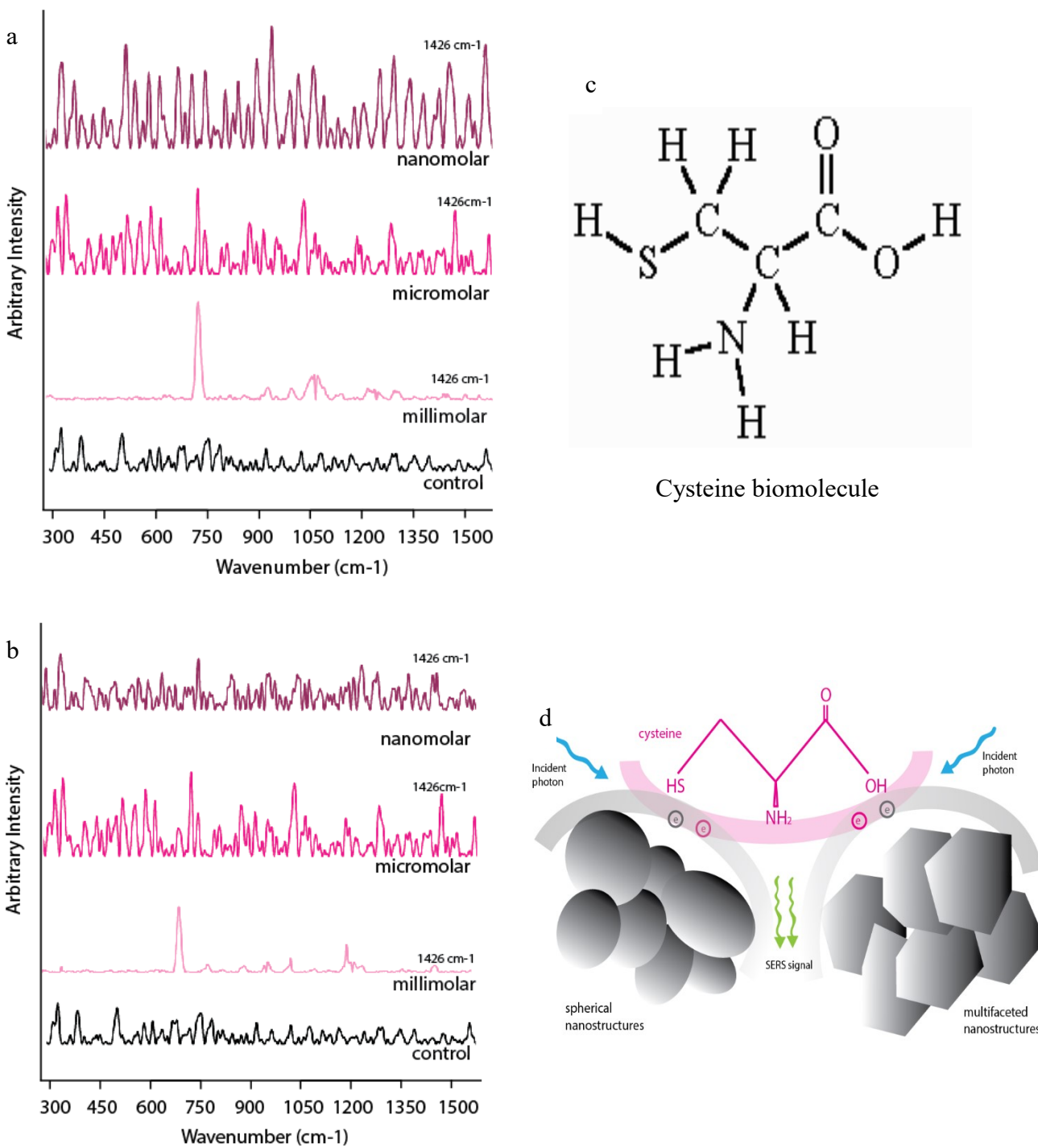


Figure 4.10 Raman spectra of cysteine adsorbed @ 532nm wavelength on a) multifaceted b) spherical Al nanostructure c) cysteine molecular structure d) SERS mechanism of cysteine adsorbed on spherical and multifaceted nanostructure

In order to test the bio-sensing ability of the sample to detect cancer cells, a biomolecule named Carcino-Embryonic Antigen (CEA) was adsorbed on the surface of the fabricated nanostructure and Raman tested for enhancement.

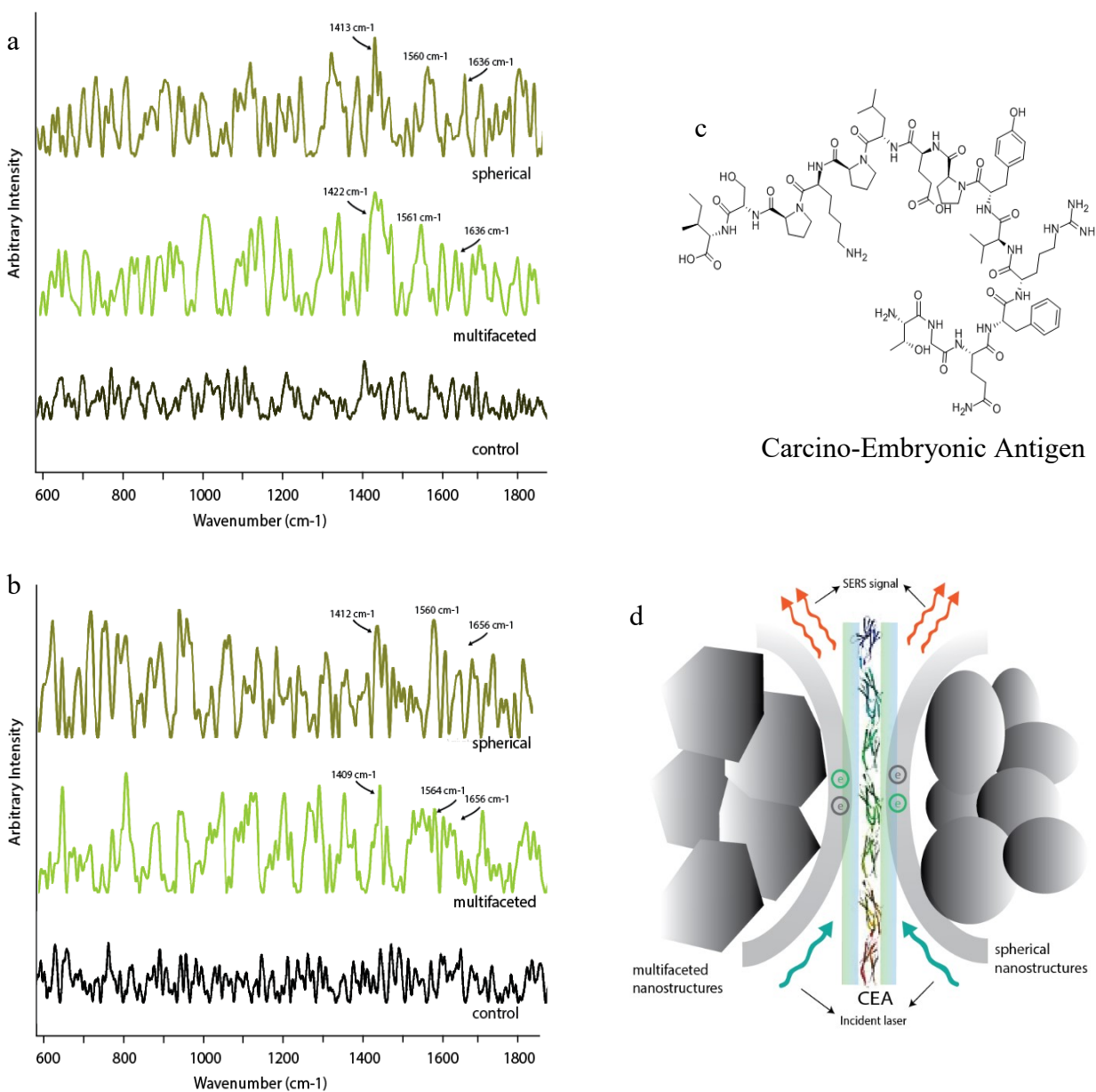


Figure 4.11 Raman spectra of CEA adsorbed on Al nanostructures of various modes @ a) 532 nm b) 785 nm c) molecular structure of CEA d) SERS mechanism of CEA adsorbed on multifaceted and spherical structures

CEA is a protein which is normally detected in our body at very low levels. The level of CEA protein tends to peak in the presence of certain types of cancer namely, lung, pancreatic, colorectal and breast cancer. Currently CEA detection test is being carried out for the detection of colorectal cancer. The ability to sense this biomolecule by our Al based nanostructures proves its viability to detect cancer in our body, thereby providing an opportunity to extend our research into invitro cancer diagnosis.

The nanostructures adsorbed with CEA were detected at two different wavelengths, 532 nm and 785nm, and seemed to have a higher enhancement factor at the 532 nm range as the material is active in that wavelength range. Also, the biological marker was tested on both the multifaceted and spherical nanostructures among which the spherical one's provided increased intensity enhancement in comparison to the multifaceted ones with respect to the control. Figure 4.1 shows the arbitrary intensity variation when CEA is adsorbed on the fabricated multifaceted and spherical nanostructures at both 532 and 785nm wavelength thereby proving multiwavelength detection. The higher enhancement at 532 also adds credibility to the surface plasmon resonance being the key factor for Raman signal enhancement. The enhancement factor calculation is carried out using equation (3). The peak at 1561 (slightly shifted due to the stresses in the structure and shape) is used to calculate the enhancement factor.

4.2 LIMIT OF DETECTION

From the previous Raman plots and the corresponding Enhancement factor comparison (Figure 4.5 and 4.8) for the 785 and 532nm wavelength and on spherical and multifaceted structure, we can see that the fabricated Aluminum based nanoparticles can detect up to femtomolar concentration (10^{-15} M) which denotes single molecule detection which to the best of our knowledge hasn't been achieved with Alumina nanostructures. This single molecule detection can be extremely useful when the Raman sensing application is extended in cell-based studies. This property is extremely useful in several applications in various disciplines including molecular nanotechnology in aerospace applications, environmental contaminants detection, non-destructive testing of illegal antibodies trafficking, etc. In this research we mainly focus on the invitro cell culturing using our fabricated Aluminum based nanoprobles to detect the presence of cancer.

4.3 SUMMARY

SERS based chemical and biosensing was tested using the fabricated 3D Aluminum based nanostructures and the corresponding mechanism responsible for the enhancement of signals were reviewed. The nanoprobe is capable of multiwavelength excitation (532 nm and 785 nm) and are able to sense chemical dyes such as CV and R6G and also biomolecules cysteine and CEA. CEA is also a cancer biomarker, which denotes the prospective of the material to detect cancer biomarker inside a cancer cell. The limit of detection is shown up to femtomolar concentration which denotes single molecule detection thereby achieving ultrasensitive detection.

CHAPTER 5 ALUMINUM BASED SERS PROBE FOR IN-VITRO CANCER DETECTION

5.1 INTRODUCTION

Cancer, being one of the leading causes of death in the world, is said to take the lives of about 16% of population of which 30% could have been saved if they've been diagnosed at an early stage. Early detection wins half the battle of the fight against cancer, as it also increases the chances of curing cancer with effective treatment. Cancer cells makes their detection tedious as they aren't recognized as a foreign body by our immune system, they are just uncontrolled growth of cells it rapidly spreads to all parts of the body. As we discussed in the previous chapter, biomarkers are molecules which expresses a biological action or any quirks in the physiological state of a cell or tissue. Cancer cells consists of biomarkers different from that of normal cells with a spike in a corresponding protein or amino acid depending on the type of cancer developed in the body. This change in the level of or the presence of a new biomarker in a cancer cell could be detected from the blood, serum, bone marrow, tissues or cells of the affected organism. A major issue of detecting these cancer biomarkers is their diminutive presence during the early stages of cancer which compels the development of technology to detect minuscule presence of biomarkers. Irrespective of gender, one of the most common type of cancer, which grows to be fatal is lung cancer followed by pancreatic cancer. If detected at an early stage, survival rate of lung cancer patients would be more than 80% in comparison to the mere 15% diagnosed with the advanced stage.

5.2 MATERIAL PREPARATION FOR CELL CULTURE

Aluminum plate purchased from McMaster was sliced in to 0.75x0.75 inch and they were first washed with ethanol to remove the impurities present on the surface and then allowed to air dry. These samples were then irradiated with ultrashort femtosecond pulsed laser to form both multifaceted nanostructures and spherical nanostructures. The fabricated substrate is then UV treated for around 15 minutes, to sterilize it of any microbes that might be present on the surface. The sample is now prepared to be seeded with the desired cell line.

5.3 CELL SEEDING AND FIXATION

Two cancer cell lines, namely the ASPC-1 (pancreatic cancer cell) and the H69 (lung cancer cell) along with a mammalian fibroblast cell line NIH3T3 were used for conducting the SERS based

experiments for the Alumina based nanoprobe. The cancer cell lines were seeded and cultured in RPMI medium whereas the fibroblasts were cultured in DMEM medium both supplemented with 10% Fetal Bovine Serum (FBS) and 10% antibiotics. The media provides the necessary nutrients for the cells to survive in vitro environment and the addition of antibiotics prevents contamination of cells from microbes during the process of cell culture. The cells were then incubated at 37 degree Celsius with 5% CO₂ until a confluency of 85% of the seeded flask was reached. Then, they undergo a process of trypsin wash which helps in removing the media, incubated with trypsin for 10 minutes to release the cells attached to the walls of the flask, centrifuged to collect the cells together and then resuspended in their respective medium to be seeded on to the prepared samples. The fabricated and UV treated Aluminum/Alumina substrate were placed in a petri-dish filled with 3ml of the respective media and the prepared cell suspended in media were then seeded on the nanostructures. The petri-dish was then incubated for various timelines namely 6, 18, 24, 48 hours at 37 degree Celsius. At the corresponding time, the samples were taken out, media removed and were washed with Phosphate-Buffered Saline (PBS), added with 4% paraformaldehyde solution to fix the cells on the sample and then incubated at room temperature for 20 minutes. The Aluminum substrate was then removed from the solution and was air dried for around 24 hours.

5.4 CELLS UNDER FLUORESCENCE MICROSCOPE

The seeded samples were imaged under fluorescence light using epi-fluorescent Nikon E-400 microscope with a green filter. This shows the growth of cells on the surface of our nanostructures and proves that our fabricated nanostructures are habitable for cell growth. Figure 5.1 shows the fluorescence images of the cells seeded on the nanostructures. It can be seen that both the spherical structure and the sharp-edged multifaceted ones provide a good environment for cell growth. The below images show the fluorescence of 3 cell lines grown on spherical and multifaceted structures.

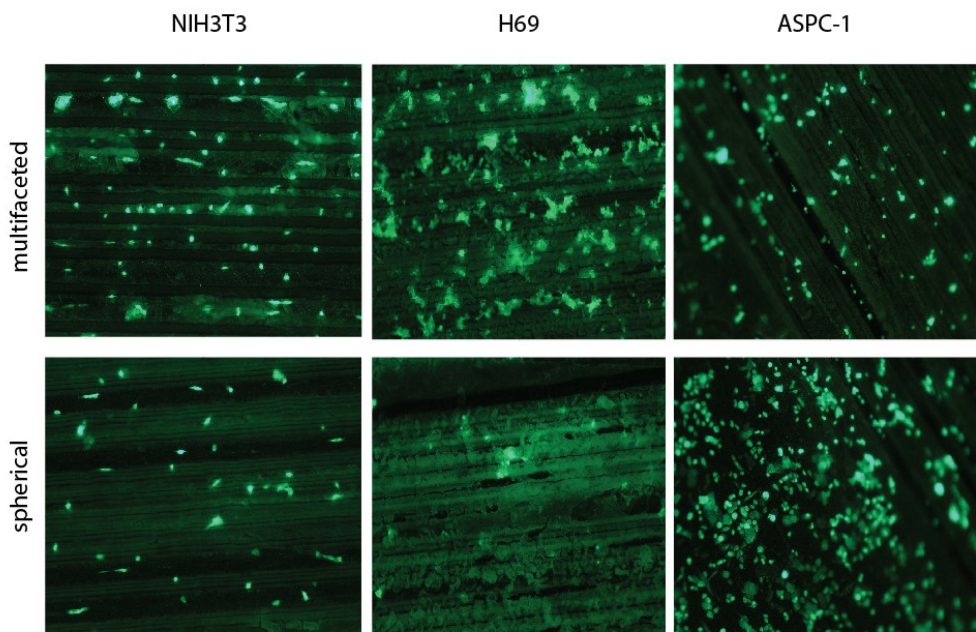


Figure 5.1 Fluorescence imaging of cells on spherical and multifaceted nanostructures

5.5 CELL SENSING USING RAMAN SPECTROSCOPY

The samples of Aluminum substrate with nanostructures were then analysed for Raman spectrum using Renishaw inVia Confocal Raman Spectrometer at multiple wavelength of 532, 633, 785nm. As the cells are said to be more stable in the 785 nm wavelength, the results with that wavelength were further analyzed and reported. Also, another reason to use 785nm is that the cells are much safer in a higher wavelength and there is a huge possibility of damaging the cells at a comparatively lower wavelength. All the obtained spectrum was plotted using ‘Spectragryph’ spectroscopy software and is shown in figure below. The figure 5.2 shows the SERS enhancement of the cells versus the corresponding Raman signals. It is thereby proved that in vitro SERS enhancement is feasible using Aluminum based nanostructures for both cancerous and non-cancerous cells. This shows that the fabricated nanostructures possess the ability to enter the cells and detect the biomarkers present in the cells. The color-coded peaks show the different intracellular components that the nanoprobe are able to detect in a cell. This also shows how the uptake of the nanoprobe into the cells are happening and the detailed time study is given below.

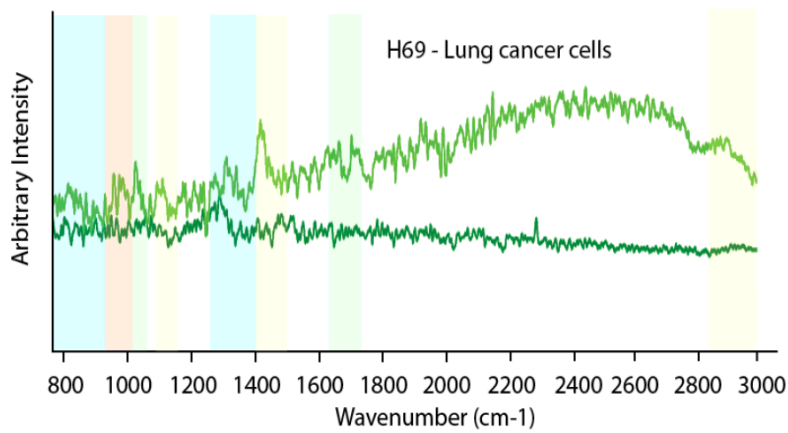
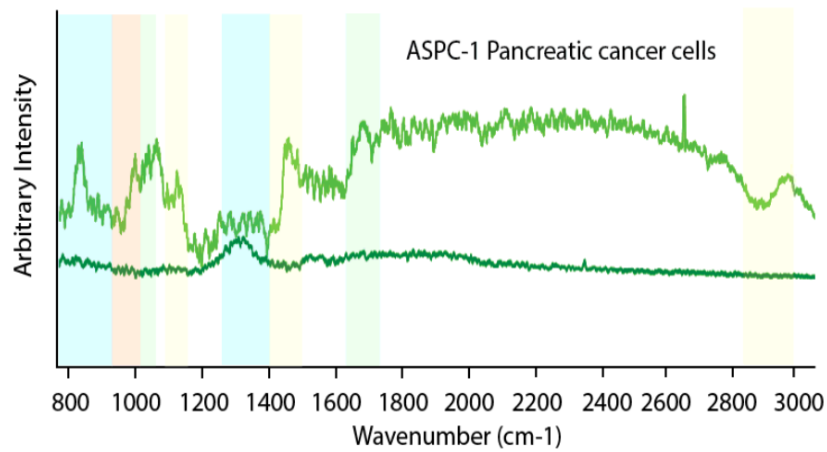
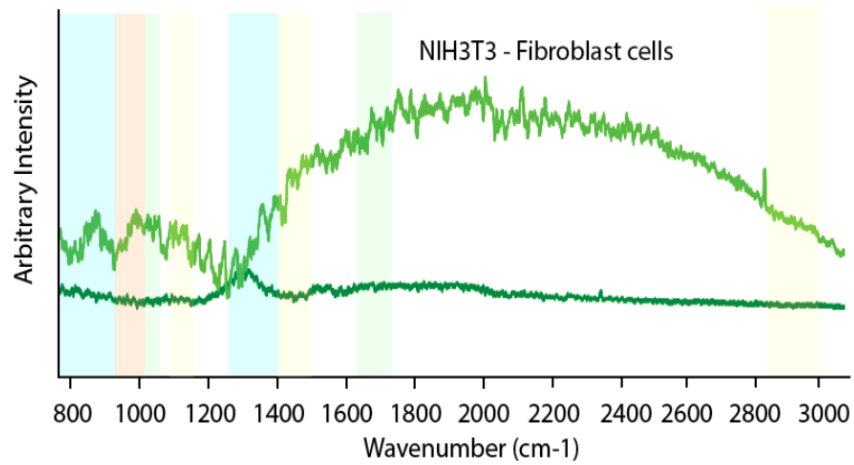


Figure 5.2 SERS signals from cells at laser wavelength of 785 nm compared with control

The Figure 5.3 Shows a comparison in the intensity of Raman spectrum between control Aluminum substrate and the multifaceted and spherical structures which further proves the sensitivity of detecting the biomarkers even in infinitesimal amount thereby being able to detect cancer at an early stage. In order to prove the materials' capability of multiwavelength sensing, the SERS spectrum obtained with 532 nm wavelength is given and further analysis were carried out with 785nm wavelength. It can be seen that when it comes to cell sensing, 785nm produces more sensitive and sharp peaks in comparison to 532 nm as in the case of the latter the cells tend to have damaged and not produce proper peaks.

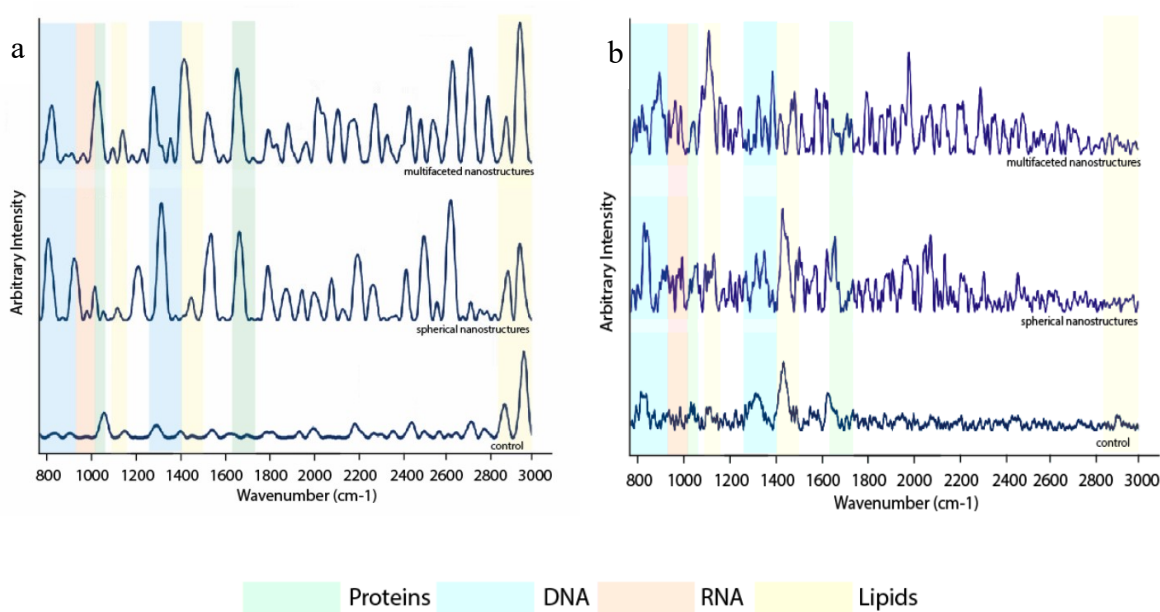


Figure 5.3 Raman spectrum of cells seeded on different shapes of nanostructures compared with the cells seeded on plain Aluminum substrate at laser wavelength of a) 532 nm b) 785 nm

5.6 TIME STUDY OF SERS IN CANCEROUS AND NON-CANCEROUS CELLS

The cell study carried out in 785nm wavelength used 4 different timelines namely 6, 18, 24 and 48 hours. These timelines were selected based on the previous studies made in the same field and that major changes in the morphological and characteristic features of cells take place at that time interval. The results indicate that the cells produce enhanced peaks until the 48th hour which shows that the cells can survive the nanoprobe until that time period.

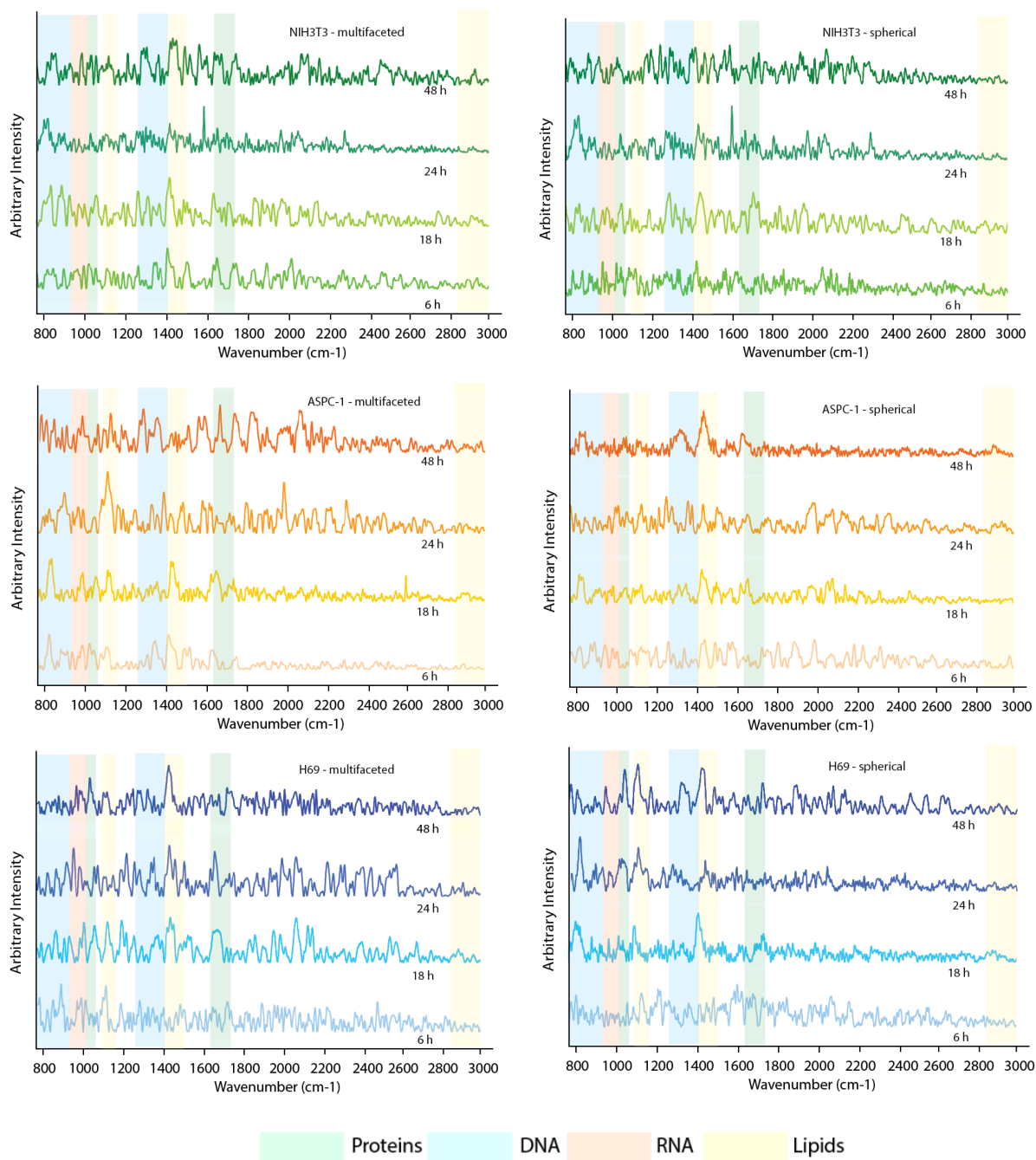


Figure 5.4 Time study carried out at 6h, 18h, 24h, and 48h for cancerous and non-cancerous cell lines seeded on multifaceted and spherical nanostructures at laser wavelength 785 nm

These individual spectra produced at varying time study for different cells lines is then compared and studying with the corresponding Raman peaks of cells from literature [26]–[31] (Refer appendix for peak assignments). The peaks corresponding with various biomolecules are then

color coded to denote their corresponding uptake and intensity. Further, ratio analysis was carried out in order to differentiate between cancerous and healthy cells.

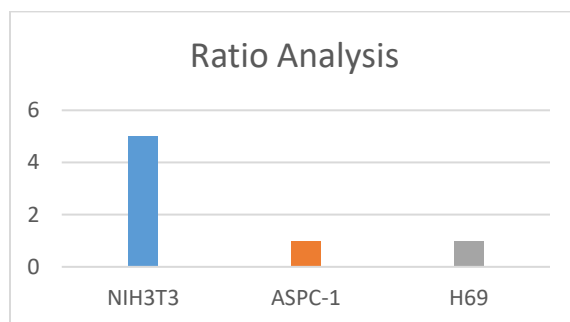


Figure 5.5 Ratio analysis for classification of cells

Figure 5.5 showcases the results of ratio analysis for healthy fibroblasts vs the lung and pancreatic cancer cells. The peaks at 1655 corresponding to C=O stretching of protein and 1445 corresponding to CH₂ scissoring of lipid are used to calculate the corresponding I_{1445}/I_{1655} ratio of lipid to protein used for ratio analysis to identify the cancerous and non-cancerous cells. The ratio of normal cells is greater than that of cancer cells and is greater than one and that of cancer cells is lesser than one. The ability to detect up to single cells using this SERS technique makes it an exciting and reliable method to perform further analysis.

5.7 SUMMARY

Three different cell lines were used for the cell-based sensing of Aluminum based nano structures. The cells were cultured and seeded on the nanomaterial which were then SERS tested. The signals obtained indicate that the nanoprobe uptake were performed by the cells which were biocompatible with the probes. The color-coded Raman spectrum indicate the various intracellular components and biomolecules the probes were able to attach themselves to and get excited. Fluorescence imaging was performed to confirm the growth of cells on the nanopatterned ablated surface. The level of detection to obtain the SERS signal was up to single cell. Further, ratio analysis was performed to differentiate the cancerous cells from the healthy mammalian cells.

CHAPTER 6 CONCLUSION AND FUTURE RESEARCH

6.1 Conclusion

This thesis presented the fabrication and characterization of an Aluminum based nanostructure with a highly sensitive Surface Enhanced Raman Sensing ability for biological and chemical sensing. The 3D nanostructure showcased unique features pertaining to its nanosize which was obtained using an ultrashort pulsed laser system with femtosecond pulses ionizing the surface of Aluminum substrate producing the nanostructures. The tunable laser system helped us in producing three unique structures of nanostructures which proclaimed their own advantages and disadvantages. These different nanostructures were then used as an active SERS material to detect dyes, biological molecules and cancer cells.

The main objective of this thesis was to synthesize 3D Aluminum based nanostructure using femtosecond laser at ambient conditions which can be used as a biocompatible probe for biosensing and in vitro cancer diagnosis. It also brings out the advantages of Aluminum/Alumina in comparison to other plasmonic metals currently being used in SERS applications and to overcome their flaws. The laser synthesis method produced materials of two unique structure – the multifaceted and spherical. Also, a third type, a mixture of multifaceted- spherical structure, were produced in the condition of Nitrogen gas atmosphere. The SERS experiments on dyes and biomolecules conferred the ability of the nanostructures to detect both chemical signals and biological markers. The specific use of a cancer biomarker further proves the affinity of the Aluminum based nanomaterials to these markers which can be found in a cancer cell and their competence to detect them. In the cellular experiments, though the multifaceted structure provided strong SERS enhancement for biosensing due to its sharp-edged corners, the spherical ones proved to be a better environment for the cells to thrive without being damaged.

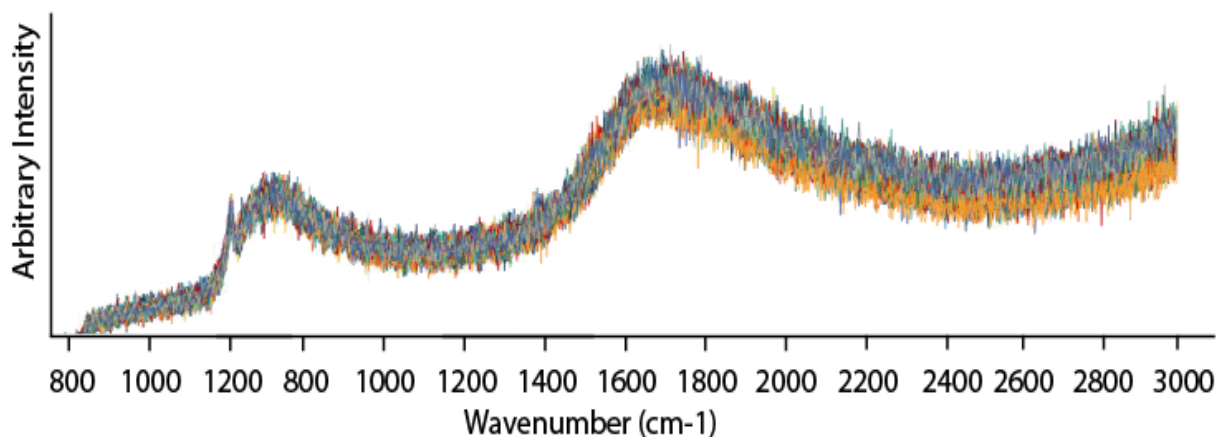
With the above results, the fabrication of Aluminum based nanostructures, their characterization and the ability to act as biological sensors and detectors have been defined and their potential are comparable to the current plasmonic metals being used in the field of research.

6.2 FUTURE RESEARCH

A novel biocompatible material was synthesized using ultrashort pulsed laser system and its characteristic properties were studied along with its application in cancer diagnostics. This research can further be extended into boundless openings to explore in addition to the progress achieved.

The research can be extended into multiple disciplines which includes optical engineering, medicine, sensor development, etc. The cell line study can further be extended to test the extension of nanoprobe uptake into the cell and toxicity study to see how longer the cells can accommodate the nanostructures. This thesis has focused on the diagnostic phase of cancer using nanoprobe whereas same method can be extended to attach drugs on to the nanoprobe to treat the detected type of cancer. We can also play around with more of the laser properties used, such as the pulse width, repetition rate, scanning speed, etc. to fabricate further different types of nanostructures with varying morphological features.

APPENDIX



A1. Time study for the fibroblast cells – 100 samples irradiated for 5 minutes

Cell peaks from literature	Peak Assignments
752	DNA, Symmetric breathing of tryptophan (protein assignment)
823	Out-of-plane ring breathing, tyrosine
855	(C-C), proline (CCH) ring breathing, tyrosine
876	(C-C), hydroxyproline
915	RNA assignment
1031	(C-H), phenylalanine
1078	(C-C) or (C-O), phospholipids
1123	(C-N), proteins
1172	(C-N), tyrosine
1208	(C-C ₆ H ₅), tryptophan, phenylalanine
1223	(PO ₂), nucleic acids
1265	(CN), (NH) amide III, alpha-helix, collagen, tryptophan
1322	CH ₃ CH ₂ twisting, collagen
1335	CH ₃ CH ₂ wagging, collagen
1445	(CH ₂) scissoring, phospholipids

1518	(C=C), carotenoid
1552	(C=C), tryptophan
1655	(C=O) amide I, alpha-helix, collagen, elastin
1745	(C=O), phospholipids
2940	C-H vibrations in lipids

A2 Table representing Raman peak assignments for cells

REFERENCES

- [1] S. K. Jha, Z. Ahmed, M. Agio, Y. Ekinici, and J. F. Löffler, “Deep-UV surface-enhanced resonance Raman scattering of adenine on aluminum nanoparticle arrays,” *J. Am. Chem. Soc.*, vol. 134, no. 4, pp. 1966–1969, 2012.
- [2] M. J. McClain *et al.*, “Aluminum Nanocrystals,” *Nano Lett.*, vol. 15, no. 4, pp. 2751–2755, 2015.
- [3] J. Martin and J. Plain, “Fabrication of aluminium nanostructures for plasmonics,” *J. Phys. D. Appl. Phys.*, no. May, p. 184002, 2015.
- [4] S. Tian *et al.*, “Aluminum nanocrystals: A sustainable substrate for quantitative SERS-Based DNA Detection,” *Nano Lett.*, vol. 17, no. 8, pp. 5071–5077, 2017.
- [5] A. S. Mahmood, K. Venkatakrishnan, and B. Tan, “3-D aluminum nanostructure with microhole array synthesized by femtosecond laser radiation for enhanced light extinction,” *Nanoscale Res. Lett.*, vol. 8, no. 1, pp. 1–8, 2013.
- [6] L. Zhou *et al.*, “3D self-assembly of aluminium nanoparticles for plasmon-enhanced solar desalination,” *Nat. Photonics*, vol. 10, no. 6, pp. 393–398, 2016.
- [7] M. J. Meziani *et al.*, “Formation and properties of stabilized aluminum nanoparticles,” *ACS Appl. Mater. Interfaces*, vol. 1, no. 3, pp. 703–709, 2009.
- [8] G. H. Chan, J. Zhao, G. C. Schatz, and R. P. V. Duyne, “Localized surface plasmon resonance spectroscopy of triangular aluminum nanoparticles,” *J. Phys. Chem. C*, vol. 112, no. 36, pp. 13958–13963, 2008.
- [9] G. Davy and K. G. Stephen, “Aluminium plasmonics,” *J. Phys. D. Appl. Phys.*, vol. 48, no. 18, p. 184001, 2015.
- [10] M. Paskevicius *et al.*, “Mechanochemical synthesis of aluminium nanoparticles and their deuterium sorption properties to 2 kbar,” *J. Alloys Compd.*, vol. 481, no. 1–2, pp. 595–599, 2009.

- [11] D. Ge, “Plasmonic Breathing and Edge Modes in Aluminum Nanotriangles,” 2017.
- [12] N. J. Halas, “Charge Transfer Plasmons : Optical Frequency Conductances and Tunable,” pp. 6428–6435, 2015.
- [13] E. Katz and I. Willner, “Integrated Nanoparticle – Biomolecule Hybrid Systems : Synthesis , Properties , and Applications Angewandte,” pp. 6042–6108, 2004.
- [14] F. Wen *et al.*, “Charge Transfer Plasmons: Optical Frequency Conductances and Tunable Infrared Resonances,” *ACS Nano*, vol. 9, no. 6, pp. 6428–6435, 2015.
- [15] M. Sivayoganathan, B. Tan, and K. Venkatakrishnan, “Synthesis of crystalline and amorphous, particle-agglomerated 3-D nanostructures of Al and Si oxides by femtosecond laser and the prediction of these particle sizes,” *Nanoscale Res. Lett.*, vol. 7, pp. 1–7, 2012.
- [16] J. M. Chem, “Fluoride-assisted galvanic replacement synthesis of Ag and Au dendrites on aluminum foil with enhanced SERS and catalytic activities †,” pp. 18327–18334, 2012.
- [17] C. L. Haynes, A. D. Mcfarland, and R. P. Van Duyne, “RAMAN SPECTROSCOPY,” 2005.
- [18] G. D. Förster *et al.*, “Oxidation-Induced Surface Roughening of Aluminum Nanoparticles Formed in an Ablation Plume,” vol. 246101, no. December, pp. 1–6, 2015.
- [19] I. Costina and R. Franchy, “Band gap of amorphous and well-ordered Al₂O₃ on Ni₃Al₁₀₀ ...,” vol. 78, no. 26, pp. 4139–4141, 2001.
- [20] H. Search, C. Journals, A. Contact, M. Iopscience, and I. P. Address, “An investigation of commercial gamma-Al₂O₃ nanoparticles,” vol. 012096.
- [21] M. Wall, “Raman Spectroscopy,” *Adv. Mater. Process.*, vol. 170, no. 4, pp. 35–38, 2012.
- [22] J. Sun, S. Wang, D. Zhao, F. H. Hun, L. Weng, and H. Liu, “Cytotoxicity, permeability, and inflammation of metal oxide nanoparticles in human cardiac microvascular endothelial cells: Cytotoxicity, permeability, and inflammation of metal oxide

- nanoparticles,” *Cell Biol. Toxicol.*, vol. 27, no. 5, pp. 333–342, 2011.
- [23] W. Ye, Y. Chen, F. Zhou, C. Wang, and Y. Li, “Fluoride-assisted galvanic replacement synthesis of Ag and Au dendrites on aluminum foil with enhanced SERS and catalytic activities,” *J. Mater. Chem.*, vol. 22, no. 35, pp. 18327–18334, 2012.
- [24] E. Katz and I. Willner, “Integrated nanoparticle-biomolecule hybrid systems: Synthesis, properties, and applications,” *Angew. Chemie - Int. Ed.*, vol. 43, no. 45, pp. 6042–6108, 2004.
- [25] E. M. Ochoa, “Air force institute of technology,” *Air Force Inst. Technol.*, 2007.
- [26] Z. Movasaghi, S. Rehman, and I. U. Rehman, “Raman spectroscopy of biological tissues,” *Appl. Spectrosc. Rev.*, vol. 42, no. 5, pp. 493–541, 2007.
- [27] Z. Huang, A. McWilliams, H. Lui, D. I. McLean, S. Lam, and H. Zeng, “Near-infrared Raman spectroscopy for optical diagnosis of lung cancer,” *Int. J. Cancer*, vol. 107, no. 6, pp. 1047–1052, 2003.
- [28] R. Haldavnekar, K. Venkatakrishnan, and B. Tan, “Non plasmonic semiconductor quantum SERS probe as a pathway for in vitro cancer detection,” *Nat. Commun.*, vol. 9, no. 1, pp. 1–18, 2018.
- [29] S. Feng *et al.*, “Nasopharyngeal cancer detection based on blood plasma surface-enhanced Raman spectroscopy and multivariate analysis,” *Biosens. Bioelectron.*, vol. 25, no. 11, pp. 2414–2419, 2010.
- [30] A. K. Misra *et al.*, “Micro-Raman spectroscopy study of ALVAC virus infected chicken embryo cells,” *Smart Biomed. Physiol. Sens. Technol. VIII*, vol. 8025, no. May, p. 80250C, 2011.
- [31] V. Canalejas-Tejero, S. Herranz, A. Bellingham, M. C. Moreno-Bondi, and C. A. Barrios, “Passivated aluminum nanohole arrays for label-free biosensing applications,” *ACS Appl. Mater. Interfaces*, vol. 6, no. 2, pp. 1005–1010, 2014.

- [32] J. Martin *et al.*, “Aluminum nanostructures for ultraviolet plasmonics,” no. August, p. 12, 2017.
- [33] P. Zhou, “Choosing the Most Suitable Laser Wavelength For Your Raman Application,” vol. 1, no. 855, p. 6, 2015.
- [34] Y. X. Pang and X. Bao, “Aluminium oxide nanoparticles prepared by water-in-oil microemulsions,” *J. Mater. Chem.*, vol. 12, no. 12, pp. 3699–3704, 2002.
- [35] R. Yahaya *et al.*, “High resolution transmission electron microscopy study of surface reconstruction on faceted cubeoctahedral γ -Al₂O₃ nanoparticles,” *EMC 2012 15th Eur. Microsc. Congr. 16-21 Sept. 2012, Manchester, United Kingdom*, no. November 2014, p. 2 pages, 2012.
- [36] Y. Rozita, R. Brydson, and A. J. Scott, “An investigation of commercial gamma-Al₂O₃ nanoparticles,” *J. Phys. Conf. Ser.*, vol. 241, p. 012096, 2010.
- [37] P. F. Liao and M. B. Stern, “Surface-enhanced Raman scattering on gold and aluminum particle arrays,” *Opt. Lett.*, vol. 7, no. 10, p. 483, 2008.
- [38] C. Zhang, A. I. Smirnov, D. Hahn, and H. Grebel, “Surface enhanced Raman scattering of biospecies on anodized aluminum oxide films,” *Chem. Phys. Lett.*, vol. 440, no. 4–6, pp. 239–243, 2007.
- [39] Z. Wei, L. Chen, D. M. Thompson, and L. D. Montoya, “Effect of particle size on in vitro cytotoxicity of titania and alumina nanoparticles,” *J. Exp. Nanosci.*, vol. 9, no. 6, pp. 625–638, 2014.
- [40] A. Gute, C. Carraro, and R. Maboudian, “2010 JACS Silver Dendrites from Galvanic Displacement on Commercial Aluminum Foil As an Effective SERS Substrate.pdf,” *J. Am. Chem. Soc.*, no. 0, pp. 1476–1477, 2009.
- [41] W. E. Doering and S. Nie, “Single-molecule and single-nanoparticle SERS: Examining the roles of surface active sites and chemical enhancement,” *Journal of Physical Chemistry B*, vol. 106, no. 2, pp. 311–317, 2002.

- [42] K. B. Mogensen *et al.*, “Surface-enhanced Raman scattering on aluminum using near infrared and visible excitation,” *Chem. Commun.*, vol. 50, no. 28, pp. 3744–3746, 2014.
- [43] G. D. Förster *et al.*, “Oxidation-Induced Surface Roughening of Aluminum Nanoparticles Formed in an Ablation Plume,” *Phys. Rev. Lett.*, vol. 115, no. 24, pp. 1–6, 2015.
- [44] J. A. Guicheteau *et al.*, “Surface-enhanced raman scattering (SERS) evaluation protocol for nanometallic surfaces,” *Appl. Spectrosc.*, vol. 67, no. 4, pp. 396–403, 2013.
- [45] P. V Thomas, V. Ramakrishnan, and V. K. Vaidyan, “35 o x i d a t i o n s t u d i e s o f a l u m i n i u m t h i n f i l m s b y r a m a n s p e c t r o s c o p y,” vol. 170, pp. 35–40, 1989.
- [46] D. Maznichenko, K. Venkatakrishnan, and B. Tan, “Stimulating multiple SERS mechanisms by a nanofibrous three-dimensional network structure of titanium dioxide (TiO₂),” *J. Phys. Chem. C*, vol. 117, no. 1, pp. 578–583, 2013.
- [47] J. A. Powell, K. Venkatakrishnan, and B. Tan, “Programmable SERS active substrates for chemical and biosensing applications using amorphous/crystalline hybrid silicon nanomaterial,” *Sci. Rep.*, vol. 6, no. August 2015, pp. 1–13, 2016.
- [48] I. M. Sadiq, S. Pakrashi, N. Chandrasekaran, and A. Mukherjee, “Studies on toxicity of aluminum oxide (Al₂O₃) nanoparticles to microalgae species: *Scenedesmus* sp. and *Chlorella* sp.,” *J. Nanoparticle Res.*, vol. 13, no. 8, pp. 3287–3299, 2011.
- [49] A. Urey-bradley, “Metal-oxygen vibration modes in the i&a-red spectra of alu~um, gallium and indium ~mace~~aceto~ates C.,” vol. 17, no. 1960, pp. 448–453, 1961.
- [50] T. Ding, D. O. Sigle, L. O. Herrmann, D. Wolverson, and J. J. Baumberg, “Nanoimprint lithography of Al nanovoids for deep-UV SERS,” *ACS Appl. Mater. Interfaces*, vol. 6, no. 20, pp. 17358–17363, 2014.
- [51] P. Colomban and G. Gouadec, “Raman Spectroscopy of Nanostructures and Nanosized Materials,” *J. Raman Spectrosc.*, vol. 38, no. May, pp. 598–603, 2007.
- [52] Y. Liu, S. Xu, H. Li, X. Jian, and W. Xu, “Localized and propagating surface plasmon co-

- enhanced Raman spectroscopy based on evanescent field excitation,” *Chem. Commun.*, vol. 47, no. 13, pp. 3784–3786, 2011.
- [53] C. L. Lay *et al.*, “Aluminum nanostructures with strong visible-range SERS activity for versatile micropatterning of molecular security labels,” *Nanoscale*, vol. 10, no. 2, pp. 575–581, 2018.
- [54] E. J. Zeman and G. C. Schatz, “An accurate electromagnetic theory study of surface enhancement factors for silver, gold, copper, lithium, sodium, aluminum, gallium, indium, zinc, and cadmium,” *J. Phys. Chem.*, vol. 91, no. 3, pp. 634–643, 1987.
- [55] R. D. Rodriguez *et al.*, “Aluminum and copper nanostructures for surface-enhanced Raman spectroscopy: A one-to-one comparison to silver and gold,” *Sensors Actuators, B Chem.*, vol. 262, pp. 922–927, 2018.
- [56] J. F. Li *et al.*, “Shell-isolated nanoparticle-enhanced Raman spectroscopy,” *Nature*, vol. 464, no. 7287, pp. 392–395, 2010.
- [57] K. Hering *et al.*, “SERS: A versatile tool in chemical and biochemical diagnostics,” *Anal. Bioanal. Chem.*, vol. 390, no. 1, pp. 113–124, 2008.
- [58] J. Gersten and A. Nitzan, “Electromagnetic theory of enhanced Raman scattering by molecules adsorbed on rough surfaces,” *J. Chem. Phys.*, vol. 73, no. 7, pp. 3023–3037, 2003.
- [59] N. Arora and B. R. Jagirdar, “Monodispersity and stability: Case of ultrafine aluminium nanoparticles (<5 nm) synthesized by the solvated metal atom dispersion approach,” *J. Mater. Chem.*, vol. 22, no. 18, pp. 9058–9063, 2012.
- [60] A. Jain *et al.*, “Magnetic-luminescent cerium-doped gadolinium aluminum garnet nanoparticles for simultaneous imaging and photodynamic therapy of cancer cells,” *J. Colloid Interface Sci.*, vol. 526, pp. 220–229, 2018.
- [61] Z. Luksiene, “Nanoparticles and their potential application as antimicrobials in the food industry,” *Food Preserv.*, pp. 567–601, 2016.

- [62] L. Braydich-Stolle, S. Hussain, J. J. Schlager, and M. C. Hofmann, "In vitro cytotoxicity of nanoparticles in mammalian germline stem cells," *Toxicol. Sci.*, vol. 88, no. 2, pp. 412–419, 2005.
- [63] D. Lin *et al.*, "Colorectal cancer detection by gold nanoparticle based surface-enhanced Raman spectroscopy of blood serum and statistical analysis," *Opt. Express*, vol. 19, no. 14, p. 13565, 2011.
- [64] H. C. Hou, Y. M. Banadaki, S. Basu, and S. Sharifi, "A Cost-Efficient Surface Enhanced Raman Spectroscopy (SERS) Molecular Detection Technique for Clinical Applications," *J. Electron. Mater.*, vol. 47, no. 9, pp. 5378–5385, 2018.
- [65] P. Villalobos and I. I. Wistuba, *Lung Cancer Biomarkers*, 1st ed., vol. 31, no. 1. Elsevier Inc., 2017.
- [66] D. L. Diab *et al.*, "NIH Public Access," vol. 6, no. 11, pp. 1249–1254, 2009.
- [67] E. Oesterling *et al.*, "Alumina nanoparticles induce expression of endothelial cell adhesion molecules," *Toxicol. Lett.*, vol. 178, no. 3, pp. 160–166, 2008.
- [68] C. Hong, S. Yang, K. W. Huang, H. Horng, and H. Yang, "DETC2011-4," pp. 1–5, 2016.
- [69] P. V. Thomas, V. Ramakrishnan, and V. K. Vaidyan, "Oxidation studies of aluminum thin films by Raman spectroscopy," *Thin Solid Films*, vol. 170, no. 1, pp. 35–40, 1989.
- [70] R. Terkeltaub, "NIH Public Access," vol. 34, no. 3, pp. 474–476, 2015.
- [71] M. Perfézou, A. Turner, and A. Merkoçi, "Cancer detection using nanoparticle-based sensors," *Chem. Soc. Rev.*, vol. 41, no. 7, pp. 2606–2622, 2012.
- [72] E. Demir, D. Burgucu, F. Turna, S. Aksakal, and B. Kaya, "Determination of TiO₂, ZrO₂, and Al₂O₃ nanoparticles on genotoxic responses in human peripheral blood lymphocytes and cultured embryonic kidney cells," *J. Toxicol. Environ. Heal. - Part A Curr. Issues*, vol. 76, no. 16, pp. 990–1002, 2013.
- [73] M. Hashimoto, J. I. Sasaki, and S. Imazato, "Investigation of the cytotoxicity of aluminum

- oxide nanoparticles and nanowires and their localization in L929 fibroblasts and RAW264 macrophages,” *J. Biomed. Mater. Res. - Part B Appl. Biomater.*, vol. 104, no. 2, pp. 241–252, 2016.
- [74] M. D., K. P., and R. K. R. V. S. S. N., “Synthesis, Characterization and Antibacterial Activity of Aluminium Oxide Nanoparticles,” *Int. J. Pharm. Pharm. Sci.*, vol. 10, no. 1, p. 32, 2018.
- [75] E. Radziun *et al.*, “Assessment of the cytotoxicity of aluminium oxide nanoparticles on selected mammalian cells,” *Toxicol. Vitro.*, vol. 25, no. 8, pp. 1694–1700, 2011.
- [76] R. A. Ismail, S. A. Zaidan, and R. M. Kadhim, “Preparation and characterization of aluminum oxide nanoparticles by laser ablation in liquid as passivating and anti-reflection coating for silicon photodiodes,” *Appl. Nanosci.*, vol. 7, no. 7, pp. 477–487, 2017.
- [77] E. J. Park *et al.*, “Biodistribution and toxicity of spherical aluminum oxide nanoparticles,” *J. Appl. Toxicol.*, vol. 36, no. 3, pp. 424–433, 2016.
- [78] A. C. Wilson, M. A. Us, H. Zhang, and S. B. Glazer, “(12) United States Patent,” vol. 2, no. 12, 2016.
- [79] S. Eliezer *et al.*, “Synthesis of nanoparticles with femtosecond laser pulses,” *Phys. Rev. B - Condens. Matter Mater. Phys.*, vol. 69, no. 14, pp. 1–6, 2004.
- [80] C. E. Aumann, “Oxidation behavior of aluminum nanopowders,” *J. Vac. Sci. Technol. B Microelectron. Nanom. Struct.*, vol. 13, no. 3, p. 1178, 2002.
- [81] H. Kim, K. M. Kosuda, R. P. Van Duyne, and P. C. Stair, “Resonance Raman and surface- and tip-enhanced Raman spectroscopy methods to study solid catalysts and heterogeneous catalytic reactions,” *Chem. Soc. Rev.*, vol. 39, no. 12, pp. 4820–4844, 2010.
- [82] K. Karlsruhe and K. E. Sickafus, “(Accepted November 1992),” vol. 1, pp. 427–437, 1992.
- [83] E. Bombardelli *et al.*, “(12) United States Patent (10) Patent No .:,” vol. 1, no. 12, pp.

- 4–6, 2001.
- [84] F. Arul Prakash, G. J. Dushendra Babu, M. Lavanya, K. S. Vidhya, and T. Devasena, “Toxicity Studies of Aluminium Oxide Nanoparticles in Cell Lines,” *Int. J. Nanotechnol. Appl.*, vol. 5, no. 2, pp. 99–107, 2011.
- [85] J. Martin and J. Plain, “Fabrication of aluminium nanostructures for plasmonics,” *J. Phys. D. Appl. Phys.*, vol. 48, no. 18, p. 184002, 2015.
- [86] A. Campos *et al.*, “Plasmonic Breathing and Edge Modes in Aluminum Nanotriangles,” *ACS Photonics*, vol. 4, no. 5, pp. 1257–1263, 2017.
- [87] T. L. Temple and D. M. Bagnall, “Optical properties of gold and aluminium nanoparticles for silicon solar cell applications,” *J. Appl. Phys.*, vol. 109, no. 8, pp. 1–13, 2011.
- [88] M. H. Chowdhury, K. Ray, S. K. Gray, J. Pond, and J. R. Lakowicz, “Aluminum nanoparticles as substrates for metal-enhanced fluorescence in the ultraviolet for the label-free detection of biomolecules,” *Anal. Chem.*, vol. 81, no. 4, pp. 1397–1403, 2009.
- [89] A. M. Polubotko and V. P. Chelibanov, “The theory of SERS on semiconductor and dielectric substrates,” *Opt. Spectrosc.*, vol. 122, no. 6, pp. 937–943, 2017.
- [90] I. Costina and R. Franchy, “Band gap of amorphous and well-ordered Al₂O₃ on Ni₃Al(100),” *Appl. Phys. Lett.*, vol. 78, no. 26, pp. 4139–4141, 2001.
- [91] R. January, “Title Thermal conductivity of graphene kirigami : ultralow and strain robustness,” pp. 1–3, 2013.
- [92] S. P. Hastings *et al.*, “Quadrupole-enhanced raman scattering,” *ACS Nano*, vol. 8, no. 9, pp. 9025–9034, 2014.
- [93] X. Wang, W. Shi, G. She, and L. Mu, “Surface-Enhanced Raman Scattering (SERS) on transition metal and semiconductor nanostructures,” *Phys. Chem. Chem. Phys.*, vol. 14, no. 17, pp. 5891–5901, 2012.
- [94] J. A. Guicheteau, A. Tripathi, E. D. Emmons, S. D. Christesen, and A. W. Fountain,

- “Reassessing SERS enhancement factors: using thermodynamics to drive substrate design,” *Faraday Discuss.*, vol. 205, pp. 547–560, 2017.
- [95] S. P. Hastings *et al.*, “Modal interference in spiky nanoshells,” *Opt. Express*, vol. 23, no. 9, p. 11290, 2015.
- [96] E. J. Liang, X. L. Ye, and W. Kiefer, “Surface-enhanced Raman spectroscopy of crystal violet in the presence of halide and halate ions with near-infrared wavelength excitation,” *J. Phys. Chem. A*, vol. 101, no. 40, pp. 7330–7335, 1997.